# Electronic, Structural and Functional Versatility in Tetrathiafulvalene-Lanthanide Metal-Organic Frameworks

Javier Castella-Gil, Samuel Mañas-Valero, Iñigo J. Vitórica-Yrezábal, Duarte Ananias, João Rocha, Raul Santiago, Stefan T. Bromley, José J. Baldoví, Eugenio Coronado, Manuel Souto, Guillermo Minguez Espallargas

Tetrathiafulvalene-Lanthanide (TTF-Ln) Metal-Organic Frameworks (MOFs) are an interesting class of multifunctional materials in which porosity can be combined with electronic properties such as electrical conductivity, redox activity, luminescence and magnetism. Herein we report a new family of isostructural TTF-Ln MOFs, denoted as MUV-5(Ln) (Ln = Gd, Tb, Dy, Ho, Er), exhibiting semiconducting properties as a consequence of the short intermolecular S···S contacts established along the chain direction between partially oxidised TTF moieties. In addition, this family shows photoluminescence properties and single-molecule magnetic behaviour, finding near-infrared (NIR) photoluminescence in the Yb/Er derivative and slow relaxation of the magnetisation in the Dy and Er derivatives. As such properties are dependent on the electronic structure of the lanthanide ion, we emphasise the immense structural, electronic and functional versatility of this class of materials.

## File list (2)

| | |
|---|---|
| Souto_Minguez_MUV-5_Manuscript.pdf (1.01 MiB) | view on ChemRxiv • download file |
| Souto_Minguez_MUV-5_SI.pdf (4.08 MiB) | view on ChemRxiv • download file |

# Electronic, Structural and Functional Versatility in Tetrathiafulvalene-Lanthanide Metal-Organic Frameworks

Javier Castells-Gil,[a] Samuel Mañas-Valero,[a] Iñigo J. Vitórica-Yrezábal,[b] Duarte Ananias,[c] João Rocha,[c] Raul Santiago,[d] Stefan T. Bromley,[d,e] José J. Baldoví,[f] Eugenio Coronado,[a] Manuel Souto*[a] and Guillermo Mínguez Espallargas*[a]

**Abstract:** Tetrathiafulvalene-Lanthanide (TTF-Ln) Metal-Organic Frameworks (MOFs) are an interesting class of multifunctional materials in which porosity can be combined with electronic properties such as electrical conductivity, redox activity, luminescence and magnetism. Herein we report a new family of isostructural TTF-Ln MOFs, denoted as **MUV-5(Ln)** (Ln = Gd, Tb, Dy, Ho, Er), exhibiting semiconducting properties as a consequence of the short intermolecular S···S contacts established along the chain direction between partially oxidised TTF moieties. In addition, this family shows photoluminescence properties and single-molecule magnetic behaviour, finding near-infrared (NIR) photoluminescence in the Yb/Er derivative and slow relaxation of the magnetisation in the Dy and Er derivatives. As such properties are dependent on the electronic structure of the lanthanide ion, we emphasise the immense structural, electronic and functional versatility of this class of materials.

## Introduction

During the last decades, the emergence of Metal-Organic Frameworks (MOFs), porous crystalline materials constructed from metallic nodes and organic linkers, has attracted a large attention in view of their limitless structural and functional versatility giving rise to a wide range of potential applications.[1] Besides their intrinsic porosity, MOFs can incorporate electronic functionalities such electrical conductivity,[2,3] magnetism[4] and luminescence[5,6] from their inorganic and organic building blocks. This permits the fabrication of novel multifunctional materials that

[a]    J. Castells-Gil, S. Mañas-Valero, Prof. E. Coronado, Dr. M. Souto, Dr. G. Mínguez Espallargas
       Instituto de Ciencia Molecular (ICMol), Universidad de Valencia
       c/ Catedrático José Beltrán 2, 46980 Paterna, Spain
       E-mail: manuel.souto@uv.es; guillermo.minguez@uv.es
[b]    Dr. I. Vitórica-Yrezábal
       School of Chemistry, University of Manchester
       Oxford Road, Manchester M13 9PL, United Kingdom
[c]    Dr. D. Ananias, Prof. J. Rocha
       Department of Chemistry and CICECO-Aveiro Institute of Materials
       University of Aveiro
       3810-193 Aveiro, Portugal
[d]    Raul Santiago, Prof. S. T, Bromley
       Departament de Ciència de Materials i Química Física & Institut de Química Teòrica i Computacional, Universitat de Barcelona, Universitat de Barcelona, C/Martí i Franquès 1, E-08028 Barcelona, Spain
[e]    Prof. S. T, Bromley
       Institució Catalana de Recerca i Estudis Avançats (ICREA), E-08010 Barcelona, Spain
[f]    Dr. J. J. Baldoví
       Max Planck Institute for the Structure and Dynamics of Matter, Luruper Chaussee 149, D-22761 Hamburg, Germany

       Supporting information for this article is given via a link at the end of the document.

combine at the same time porosity with various physical properties.[7]

Tetrathiafulvalene(TTF)-based ligands are promising building-blocks for obtaining such materials since they can provide interesting features such as electrochemical properties or electrical conductivity.[8] TTF derivatives show a remarkable electron-donor character and they can form π-π stacks with relatively short S···S interactions to promote charge transport. For this reason, these systems have been widely studied as molecular conductors in the field of molecular electronics. In recent years, a variety of TTF-based MOFs have been reported to exhibit tunable electrical conductivity,[9,10] photo-induced spin-crossover,[11] enhanced catalytic activity[12] or breathing-dependent redox activity.[13,14]

On the other hand, lanthanide Metal-Organic Frameworks (Ln-MOFs) have also attracted a broad interest since they can exhibit interesting structural and chemical properties including magnetism and luminescence.[15] For example, trivalent lanthanide ($Ln^{3+}$) MOFs exhibiting photoluminescence are promising materials with numerous applications for the development of sensors and light-emitting devices.[5,6] In addition, the incorporation of single-molecule magnetic (SMM) behaviour into a family of Ln-MOFs has been recently accomplished through the use of anisotropic magnetic ions[16,17] making these materials very interesting candidates for quantum computation and molecular spintronic applications[18].

In the last years, Pointillart *et al.* have described a variety of lanthanide coordination complexes bearing different TTF ligands which can exhibit multiple functionalities such as luminescence, redox properties and SMM behaviour.[19–21] In addition to their intrinsic redox properties, TTF-based ligands can act as both structural agent and organic chromophore isolating the magnetic centres and sensitising the lanthanide luminescence.[20] In this context, the three-dimensional organisation of these TTF-Ln complexes is encouraged in order to incorporate further functional properties such as electrical conductivity taking advantage of intermolecular interactions between partially oxidised TTF units.[9,22,23]

Along this line, two different TTF-Ln MOFs families exhibiting semiconducting and magnetic properties have been very recently reported.[23,24] However, the crystal structures of these materials show the formation of orthogonal TTF dimers or large intermolecular S···S distances, which are usually problematic for attaining a proper orbital overlap between the TTF moieties and, thus, limiting the charge delocalization. Herein, we present a family of isostructural TTF-Ln MOFs, achieved by an alternative synthetic procedure and named as **MUV-5(Ln)** (MUV: Materials of University of Valencia; Ln = Gd, Tb, Dy, Ho, Er), yielding a new crystal structure in which the TTF moieties are arranged in a parallel fashion and with relatively short S···S interactions enhancing the electronic coupling between TTF units, as

confirmed by transfer integral calculations. The TTF linkers are partially oxidised being responsible for charge transport and for the semiconducting behaviour of the MOF. In addition, photoluminescence properties and SMM behaviour have been studied for **MUV-5**. Such properties are dependent on the electronic nature of the lanthanide ion[26], evidencing a wide structural, electronic, and functional versatility for this new family of TTF-Ln MOFs.

## Results and Discussion

### Synthesis

**MUV-5(Ln)** was synthesised by means of an isoreticular approach through an adapted synthetic procedure described for the synthesis of MUV-4(Dy).[17] Solvothermal reaction of $Ln(OOCCH_3)_3$ and TTF-tetrabenzoic acid ($H_4TTFTB$) in a mixture of water and acetic acid at 170 °C for 12 hours allowed the formation of single-crystals of **MUV-5** (Scheme 1). Two crystalline polymorphs were identified by Single-Crystal X-Ray Diffraction (SCXRD), namely **MUV-5a** and **MUV-5b**, of formulae $[Ln_3(TTFTB)_2(OOCCH_3)(OH)(H_2O)]\cdot2.5H_2O$[27] and $[Ln(HTTFTB)(H_2O)]\cdot(CH_3COOH)$, respectively, whose formation depends on the amount of acetic acid used in the synthesis.
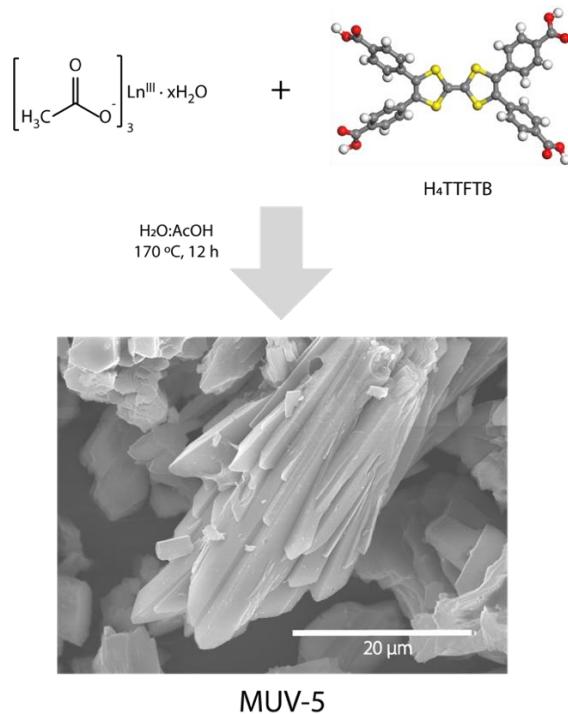


**Scheme 1**. Synthesis of **MUV-5a**

### Crystal structure

**MUV-5a** crystallises in the monoclinic space group $P2/c$ (Tables S1 and S2). Two crystallographically independent $Ln^{3+}$ ions are found in the asymmetric unit with different coordination environments. One of them is 7-coordinated with a capped trigonal prism geometry, whereas the second $Ln^{3+}$ ion can be either 8 or 9-coordinated with a distorted triangular dodecahedron environment and spherical capped square antiprism, respectively, as calculated by the software SHAPE[25] (Figures S1 and S2). The difference between the 8 or 9-coordinated form in the latter relies on the position of the disordered acetate anion acting as a bridge between both $Ln^{3+}$ ions (Figure 1b). The metallic secondary building unit (SBU) is composed of $Ln^{3+}$ ions connected through bridging carboxylate bonds from the linker and acetate anions to form infinite Ln-carboxylate chain along the $a$-axis. The connection of these infinite Ln-carboxylate chains with the TTFTB linkers yields a 3D structure with two types of parallel 1D micropores extending along the $a$-axis that are filled with water molecules or coordinated acetate anions (Figure 1).
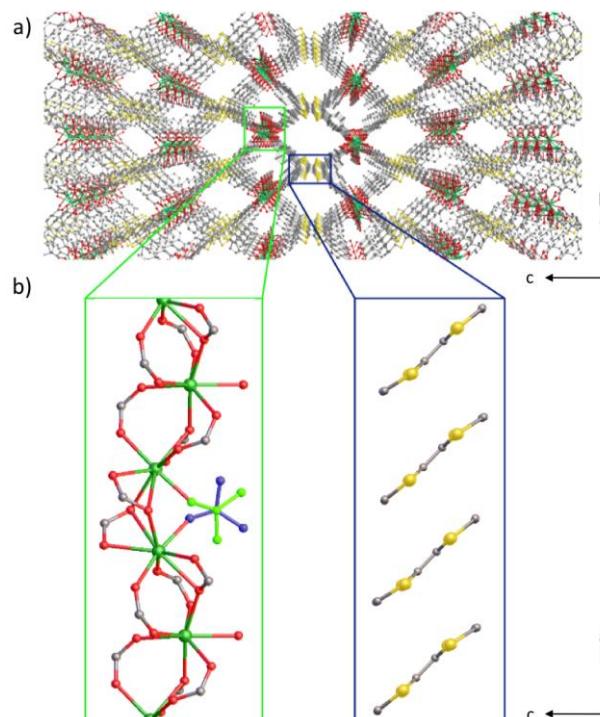


**Figure 1**. a) View of the crystal structure of **MUV-5a** along the $a$-axis and b) view of the arrangement of the $Ln^{3+}$ ions (left) and TTF units (right) within the structure of **MUV-5a**. Colour code: C (grey), O (red), Ln (green), S (yellow)**.** The disordered acetate anions have been highlighted as green and blue in order to show the two different orientations of the acetate molecules.

On the other hand, **MUV-5b** crystallizes in the monoclinic space group $P2_1/n$. Unlike **MUV-5a**, **MUV-5b** has a dimeric $Ln_2$ SBU similar to that observed in MUV-4a[17]. In this case, only one crystallographically independent $Ln^{3+}$ ion is observed in the

asymmetric unit. Each Ln atom is 8-coordinated with a distorted triangular dodecahedron geometry (Figures S3 and S4). The structure of **MUV-5b** is built upon dimeric SBUs of formula $[Ln_2(H_2O)_2(\mu\text{-}O_2C)_2(O_2C)_4(HO_2C)_2]$ (Figure S5) in which the $Ln^{3+}$ ions are kept at a distance of 4.88 Å connected by two bridging carboxylate groups. The coordination sphere of each $Ln^{3+}$ ion is completed by other 5 oxygen atoms from 3 different carboxylate groups and one water molecule (Figure S5). Finally, structure of **MUV-5b** also displays two types of one-dimensional micropores filled with acetic acid (Figure S3).

Pure crystalline phase of **MUV-5a** was confirmed by Powder X-Ray diffraction (PXRD, Figures S7-S12) and Thermogravimetric Analysis (TGA) (Figure S13). LeBail refinement converged with very good residual values ($R_{wp}$ = 5.58 %; $R_p$ = 4.36 %, Figure S8, Table S3). The small one-dimensional micropores allow the structure to have a free volume of 24 % of the unit cell volume as calculated by Mercury[28] (Figure S14). In order to examine the porosity of these materials, gas sorption experiments were performed on **MUV-5a** which was previously activated at 150 ºC under vacuum overnight. $N_2$ adsorption-desorption isotherms performed at 77 K reveals a minimum uptake of $N_2$, in line with other previously reported TTF-based coordination polymers.[29] Interestingly, **MUV-5a** is able to adsorb $CO_2$ with a modest $CO_2$ uptake of 65 $cm^3 \cdot g^{-1}$ (12.8 wt. %) at 273 K (Figure S15), which is higher than that observed in other similar TTF-based MOFs at 195 K[29], and a total uptake of 2.1 $mmol \cdot g^{-1}$ at 12 bar and 273 K (Figure 2). The selectivity of **MUV-5a** towards the adsorption of $CO_2$ over $N_2$ likely arises from the higher quadrupole moment of $CO_2$, which makes it capable of interacting more strongly with the framework.[29,30] This feature opens the way for the utilization of this type of materials in gas separation or sensing applications.
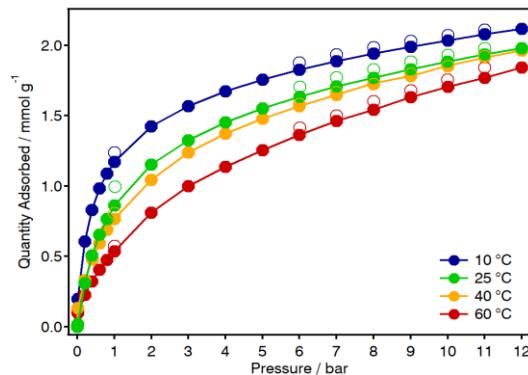


**Figure 2.** Adsorption (closed symbols) and desorption (open symbols) isotherms of $CO_2$ at different temperatures in **MUV-5a(Dy)**.

As far as the arrangement of the organic linkers is concerned, we note that in **MUV-5** solids the TTF units are forming one-dimensional segregated stacks of slightly slipped moieties running along the *a*-axis (Figures 1 and 3). However, there are important differences in both structures. First, the TTF struts in **MUV-5b** display a boat conformation with a central C=C distance of 1.32 Å and the dihedral angle between the planes formed by the two dithiol rings is 17˚ (Figure S6), suggesting that the TTF moiety is in the neutral state[31,32] (Figure 3a). On the other hand, the TTF moieties are packed along the *a*-axis with inter-centroid and S···S distances ranging from 4.40-4.90 Å and 3.92-4.27 Å, respectively. In contrast, in **MUV-5a** the TTF units adopt an S-shaped conformation with a central C=C bond distance of 1.34 Å, which is slightly longer than that in **MUV-5b** (Figure 3) and a dihedral angle of 5˚, suggesting that the TTF units in **MUV-5a** are in the radical cation state (i.e. as TTF•+), or at least partially oxidised. It is important to note that neutral TTF has a boat-like conformation ($C_{2v}$ symmetry) whereas TTF•+ moieties have a planar $D_{2h}$ symmetry as a result of the 6 $\pi$-electron heteroaromaticity of the 1,2-dithiolium cation.[32,35] The partial oxidation of the TTF units in **MUV-5a** was confirmed by EPR measurements of the crystals at room temperature that show a signal with a $g$ = 2.007, characteristic of organic radicals, and much more intense than the one for **MUV-5b** (Figure S16). As it has been observed in similar systems, TTF moieties in **MUV-5a** were at least partially oxidised during the MOF synthesis.[9] We hypothesise that this excess of positive charge is compensated through deprotonation of coordinated water molecules. Otherwise, the TTF units are stacked in a parallel manner nearly equally separated with inter-centroid distances ranging from 4.06 to 4.28 Å and being the closest S···S distances 3.61 and 3.86 Å (Figure 3b). These distances between the TTF units in **MUV-5a** are significantly shorter than in **MUV-5b**, and comparable to other TTF-based MOFs that display electrical conductivity.[9,10] This different arrangement with shorter intermolecular interactions between the partially oxidised TTF units in **MUV-5a** should be translated in a better orbital overlap between the linkers and, thus, in an enhancement in the conducting properties of the material that will be discussed below.
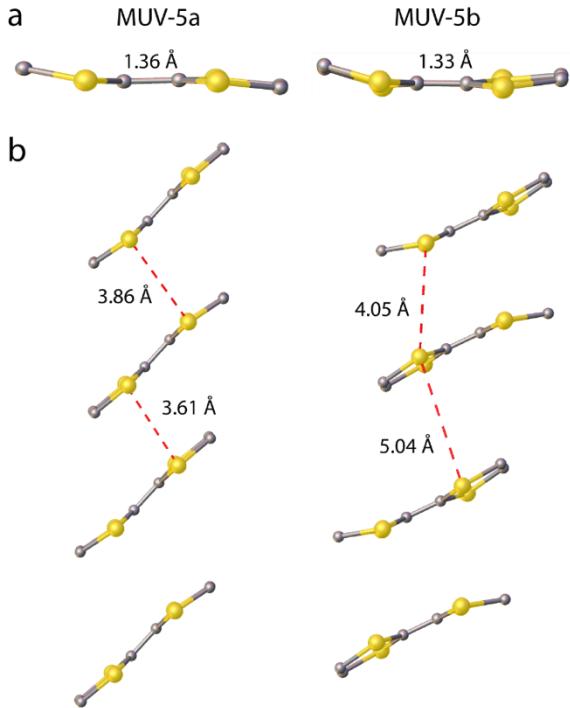
**Figure 3**. View of the a) conformation and b) arrangement of the TTF units within the structure of **MUV-5a** and **MUV-5b.** The red dashed lines show the shortest S···S distances between TTF pairs in **MUV-5(Dy)**.

Charge values for the TTF moieties in each structure were estimated by taking into account the bond length (C=C/C-S) ratio[34] obtaining values in the range from +0.1 to +0.7 suggesting that the TTF units are partially charged in **MUV-5a** (Table S5) in agreement with EPR spectroscopy. By contrast, the charge calculated in the case of **MUV-5b** indicate that TTF units are in the neutral state (q = 0). It should be noted that this correlation between charge and geometry is only approximate, although the estimated charges are in good agreement with the more planar conformation of the TTF units in **MUV-5a** (dihedral angle of 5˚), which is typical for TTF$^{+\cdot}$ radical cation, whereas the boat-like conformation in **MUV-5b** (dihedral angle of 17˚) is similar to the one for neutral TTF.[32,35]

|  | Conductivity (S·cm$^{-1}$) [a] | Shortest S···S distances (Å) |
|---|---|---|
| **MUV-5a(Gd)** | $2.0 \times 10^{-7}$ | 3.73 |
| **MUV-5a(Tb)** | $1.5 \times 10^{-5}$ | 3.68 |
| **MUV-5a(Dy)** | $3.9 \times 10^{-7}$ | 3.61 |
| **MUV-5a(Ho)** | $6.7 \times 10^{-6}$ | 3.67 |
| **MUV-5a(Er)** | $7.4 \times 10^{-6}$ | 3.65 |
| **MUV-5b(Dy)** | $3.3 \times 10^{-7}$ | 4.05 |

[a] Conductivities measured using four-contact probe pressed pellets at room temperature of two independent samples. Errors in the Supporting Information.

**Electrical conductivity**

In view of the formation of parallel stacks and partial oxidation of the TTF linkers which could promote charge transport in **MUV-5a(Ln)**, transport measurements of the different samples were performed using four-contact probe pressed pellet devices from two independent batches (see Supporting Information for more information). The room temperature conductivities for **MUV-5a(Gd), MUV-5a(Tb)**, **MUV-5a(Dy)**, **MUV-5a(Ho)** and **MUV-5a(Er)** were found to be in the order of $10^{-5} - 10^{-7}$ S·cm$^{-1}$ (see Table S4 and Figures S18-S29). Although ground boundaries in pressed pellets induce large resistance in comparison to single crystal measurements, the obtained values are comparable to the ones for other TTF-based MOFs also measured as pressed pellets[33] and around two orders of magnitude higher than those for a recently reported TTF-Ln MOF family which show similar electrochemical properties (Figure S30).[25] It is important to note that in our case electrical conductivity is achieved without the need of any doping process since TTF moieties are already partially oxidised during the synthesis, thus maintaining permanent porosity in the structures. On the other hand, electrical conductivity for **MUV-5b(Dy)** was measured to be in the order of $10^{-8}$ S·cm$^{-1}$, one order of magnitude lower than for **MUV-5a(Dy)** which is consistent with the presence of larger S···S intermolecular distances and the absence of oxidised TTF units.

**Transfer integral calculations**

In order to further understand the difference of conductivities in **MUV-5a** and **MUV-5b**, DFT based calculations of intermolecular transfer integrals for TTF units in **MUV-5** were performed. Transfer or hopping integrals ($t$) measure the overlap of the frontier orbitals (i.e. HOMOs or LUMOs) between adjacent molecules and thus provide an indication of the strength of intermolecular conduction pathways for electrons (for HOMOs) or holes (for LUMOs). These calculations were performed using the Gaussian09 package [36] employing the PBE0 [37] and B3LYP [38] hybrid functionals, with a 6-311+G(d,p) basis set. Transfer integrals between the TTF moieties in the MOFs were calculated in free space with no intervening metals at 0 K providing information about the overlap between the molecular orbitals of the TTF units through which charge transport is expected to occur. Calculations using both functionals provided consistent and comparable results (see Table S6) and we report B3LYP values hereafter. The transfer integrals for neutral **MUV-5a** were calculated to be $t_1$ = 90.6 and $t_2$ = 16.5 meV which are considerably higher than the ones for **MUV-5b** ($t_1$ = 60.5 and $t_2$ = 8.4 meV) (Figure 4) in agreement with the higher conductivity measured for **MUV-5a**. We have also compared these values with the ones calculated for the other two TTF-Ln systems reported by Dincă[24] and Zuo[25] in order to examine potential correlations between the calculated transfer integrals and measured electrical conductivities. Regarding the systems reported by Dincă,[24] the

transfer integral was calculated to be 86.1 meV between the TTF dimers. However, the transfer integrals are significantly lower (32.9 and 12.9 meV) between orthogonally displaced non-dimerised TTF units (see Figure S31) in this system. On the other hand, although in the family of materials reported by Zuo and co-workers[25] the TTF units are displaced in a parallel fashion, the transfer integrals are lower (61.5 and 48.6 meV) than those for **MUV-5a**. This difference could help to explain the lower electrical conductivity reported by Zuo *et al.* ($10^{-8}$ – $10^{-9}$ S·cm$^{-1}$) as compared to that measured for **MUV-5a** ($10^{-6}$ – $10^{-7}$ S·cm$^{-1}$).
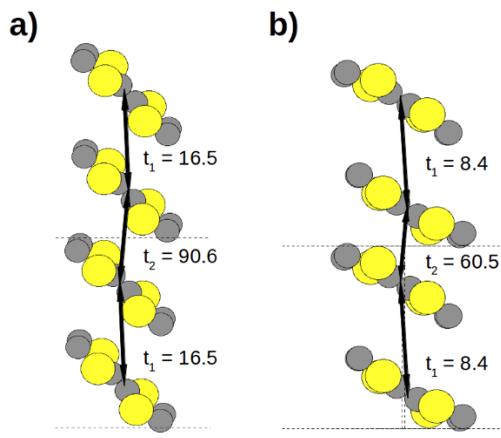


**Figure 4.** Schematic representation of TTF arrangements in the crystal structures of a) **MUV-5a** and b) **MUV-5b** indicating the transfer integrals (in meV).

## Photoluminescence properties

To analyse the possible enhancement of photoluminescence via energy transfer among different lanthanide ions,[39] the mixed-lanthanide **MUV-5a(Yb$_{0.76}$Er$_{0.24}$)** was synthesized and characterized (see Supporting Information). The excitation spectra of **MUV-5a(Yb$_{0.76}$Er$_{0.24}$)**, **MUV-5a(Er)** and **MUV-5a(Gd)** compounds recorded at 295 K and 12 K (Figure 5) display a broad band from 250 to ca. 675 nm ascribed to the TTFTB$^{4-}$ organic linker, covering most of the ultraviolet and visible spectral range. The spectra of **MUV-5a (Yb$_{0.76}$Er$_{0.24}$)** further display intense sharp lines in the 920-980 nm range assigned to the $^2F_{7/2} \rightarrow ^2F_{5/2}$ transition of Yb$^{3+}$. The poorer signal-to-noise ratio of **MUV-5a(Er)** sample spectra indicate that TTFTB ligand is more suited to sensitize Yb$^{3+}$ than the Er$^{3+}$ via the energy transfer process known as 'antenna effect'. Moreover, the Yb$^{3+}$ emission may also be activated by direct excitation.
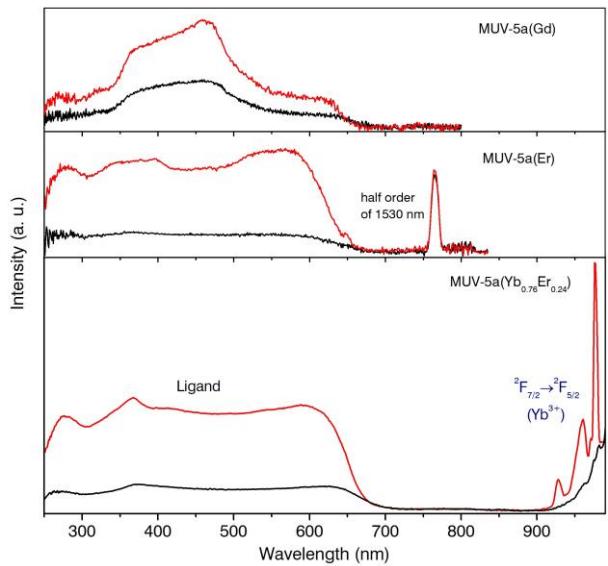


**Figure 5.** Excitation spectra of **MUV-5a (Yb$_{0.76}$Er$_{0.24}$)** ($\lambda_{Em.}$ = 1040 nm), **MUV-5a(Er)** ($\lambda_{Em.}$ = 1530 nm) and **MUV-5a(Gd)** ($\lambda_{Em.}$ = 1020 nm) recorded at 295 K (black lines) and at 12 K (red lines).

Upon ligand-mediated excitation at 560 nm, **MUV-5a(Yb$_{0.76}$Er$_{0.24}$)** (Figure 6) shows both intense emission in the 980-1050 nm region assigned to the Yb$^{3+}$ $^2F_{5/2} \rightarrow ^2F_{7/2}$ transition, and faint emission peaking at 1530 nm assigned to the Er$^{3+}$ $^4I_{13/2} \rightarrow ^4I_{15/2}$ transition. At 12 K, the well-defined sharp Stark components, resulting from the crystal-field splitting of the emitting states, demonstrate the crystallinity of the sample. Under the same excitation conditions, the emission of **MUV-5a(Er)** (Figure 6) is clearly weaker and dominated by a broad band ranging from *ca.* 940 to 1250 nm; the Er$^{3+}$ $^4I_{13/2} \rightarrow ^4I_{15/2}$ transition is only prominent at 12 K. Because it is also present in the **MUV-5a(Gd)** spectra (Figure 6), the former band is attributed to the ligand's emission. The effective sensitization of the Yb$^{3+}$ over the Er$^{3+}$ emission is mainly due to a larger overlap between the ligand emission and the Yb$^{3+}$ $^2F_{5/2}$ excited state, with an expected absorption cross-section at its maximum (976 nm) seven times larger than the resonant 980 nm Er$^{3+}$ $^4I_{11/2}$ level.[40] The larger Yb$^{3+}$ cross-section is often used to improve the Er$^{3+}$ emission via Yb$^{3+}$-to-Er$^{3+}$ energy transfer, including in Ln-bearing MOFs.[41,42] This is not observed for **MUV-5a(Yb$_{0.76}$Er$_{0.24}$)** presumably due to an effective quenching of the Er$^{3+}$ emission prompted by the C-H, N-H and O-H high energy vibrations of the ligand and free water molecules. Such quenching effect is more relevant for the Er$^{3+}$ emission because the energy gap between the corresponding emitting and fundamental level is significantly smaller, ca. 6510 cm$^{-1}$ *vs.* 10200 cm$^{-1}$ for Er$^{3+}$ and Yb$^{3+}$, respectively. The 295 K and 12 K Yb$^{3+}$ emission lifetime in **MUV-5a(Yb$_{0.76}$Er$_{0.24}$)** are 7±1 and 12±1 μs, respectively (Figure S33 in the Supporting Information).
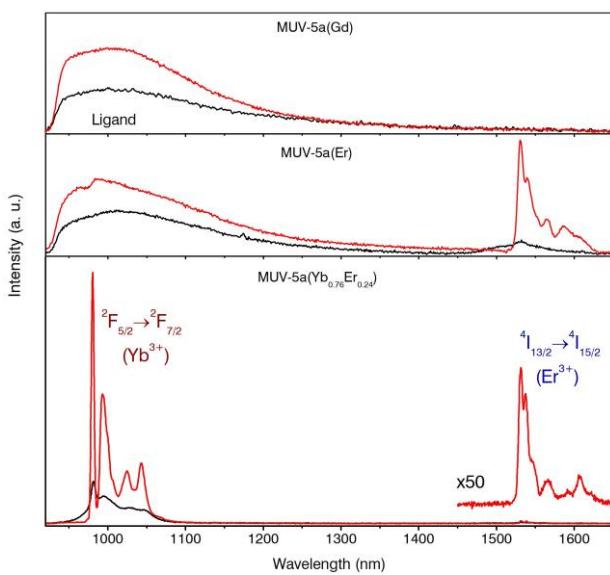
**Figure 6.** Emission spectra of **MUV-5a(Yb$_{0.76}$Er$_{0.24}$)** ($\lambda_{Exc.}$ = 560 nm), **MUV-5a(Er)** ($\lambda_{Exc.}$ = 560 nm) and **MUV-5a(Gd)** ($\lambda_{Exc.}$ = 430 nm) recorded at 295 K (black lines) and at 12 K (red lines).

## Magnetic properties

Static magnetic measurements (dc) of **MUV-5a** solids were performed between 2 and 300 K under an applied field of 1000 G. The $X_mT$ values at room temperature of **MUV-5a** are close to those expected for the free Ln ion, which indicates that most of the energy levels are populated at room temperature (Figure 7). The drop observed in $X_mT$ at low temperatures is primarily ascribed to the depopulation of the highest energy levels, which is characteristic of anisotropic lanthanide ions. In case of **MUV-5a(Er)** there is a slight increase below 7 K, which may indicate the presence of weak dipolar ferromagnetic interactions.

The static magnetic susceptibility was simulated using the Radial Effective Charge[43] model, as implemented in the SIMPRE[44] computational package (See ESI for details), for all the **MUV-5a** solids. The full set of crystal field parameters, ground-$J$ multiplet energy level schemes and main contributions to the wave functions are reported in Tables S8-12. According to our calculations, the predicted ground state for **MUV-5a(Dy1)** is mainly composed by |±1/2> (98.7%), whereas **MUV-5a(Dy2)** is characterized by 80% of |±15/2>. This means that, in the case of Dy, the second crystallographic centre is the one responsible of the observed SMM behaviour. This situation is dissimilar to **MUV-5a(Er)**, where both crystallographic centres have a ground doublet characterized by high spin microstates (80.1% |±13/2> + 11.7% |±15/2> in the case of **Er1,** and 66.6% |±15/2> + 19.0% |±9/2> for **Er2**). However, the energy difference between the ground state and the first excited state in both centres is ~11 and 25 cm$^{-1}$, for **Er1** and **Er2**, respectively, which together with molecular and lattice vibrations may limit the performance of these systems as molecular nanomagnets.[45] On the other hand, the ground state of the different magnetic centres of **MUV-5a(Tb)**

and **MUV-5a(Ho)** are mainly characterized by |0> or a heavy mixture in the case of **Ho1**, which suggests the presence of fast relaxation processes.
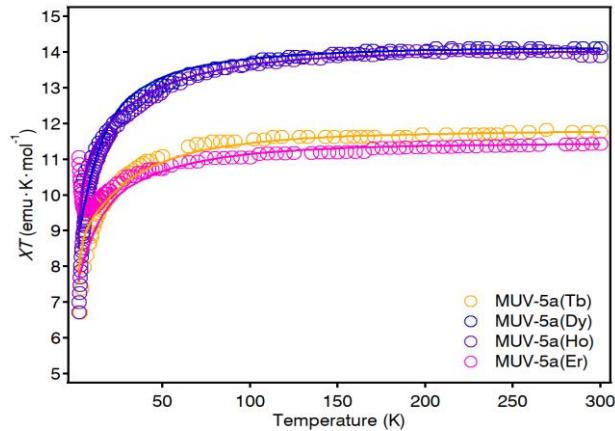


**Figure 7.** Experimental data (symbols) and theoretical simulation (lines) of the temperature dependence from 2 to 300 K of the magnetic susceptibility of **MUV-5a**. Tb (yellow), Dy (blue), Ho (purple) and Er (pink).

In order to demonstrate the differences in the magnetic behaviour of the different **MUV-5a** solids, we carried out dynamic (ac) magnetic measurements. As expected for **MUV-5a(Tb)** and **MUV-5a(Ho),** no out-of-phase signal ($X''$) can be observed at frequencies as high as 1000 Hz, even after applying an external dc magnetic field of 1000 G. In contrast, a frequency dependent out-of-phase signal is observed for **MUV-5a(Dy)** and **MUV-5a(Er)** as anticipated by the theoretical calculations (Figures S34 and S35). This is in agreement with the magnetic properties observed in similar Ln-MOFs.[25] However, no maximum in the out-of-phase signal can be observed above 2K, likely due to the presence of a very fast relaxation of the magnetization through a quantum tunnelling mechanism, as it has been previously suggested for other MOFs showing SMM behaviour.[17]

## Conclusions

In summary, we have reported a new family of isostructural TTF-Ln MOFs, denoted as **MUV-5(Ln)**, which shows enhanced electrical semiconducting properties due to an effective 1D packing of the TTF moieties as confirmed by transfer integral calculations. In addition, near-infrared photoluminescence and slow relaxation of the magnetisation were investigated in different **MUV-5** solids which can be finely tuned by suitable choice of the Ln ions, thus giving rise to a new family of versatile functional MOFs showing different properties within the same material at the same time. Current research is focused on the synergism between different physical properties, such as conductivity and luminescence, as well as on the influence of the trapped molecules on these physical properties. We are confident that our findings will help to broaden the family of MOF featuring tailored functionalities.

# Experimental Section

**Synthesis of MUV-5(Ln):** Common synthesis of **MUV-5** solids were carried out by suspending 16.5 µmol of $Ln(CH_3COO)_3 \cdot xH_2O$ and 12.5 µmol of $H_4TTFTB$[12] in a mixture of 1.3 mL of $H_2O$ and 0.7 mL of AcOH (**MUV-5a**) or 1.5 mL of $H_2O$ and 0.5 mL of AcOH (**MUV-5b**) in a 4 mL glass vial. The vial was sealed and sonicated for a few minutes to get a homogeneous suspension. The dark suspension was subsequently heated in an oven at 170 ºC for 12 hours (↑ +2.0 ºC min$^{-1}$, ↓ −0.4 ºC min$^{-1}$). After cooling down to room temperature, the dark red crystals were recovered by centrifugation and rinsed with fresh DMF, water and MeOH several times. The solid was then allowed to dry in air at room temperature, and was further heated at 150 ºC for at least 2 hours in order to yield activated **MUV-5a**. Anal. Elem. **MUV-5a** $[Dy_3(C_{34}H_{16}O_8S_4)_2(OOCCH_3)(OCHN(CH_3)_2)] \cdot (OCHN(CH_3)_2)$: Calcd.: C, 44.44; H, 2.40; S, 12.49; N, 1.36. Found: C, 45.05; H, 2.68; S, 12.37.; N, 0.99. **MUV-5b** $[Dy(C_{34}H_{16}O_8S_4)(H_2O)](CH_3COOH)$: Calcd.: C, 46.93; H, 2.41; S, 13.92. Found: C, 46.96; H, 2.67; S, 13.17.

General methods and materials, crystal data, chemical characterisation, electrical measurements, transfer integral calculations, photoluminescence, magnetic measurements and calculations are available in the Supporting Information.

# Acknowledgements

**Keywords:** Metal-Organic Framework • Tetrathiafulvalene • Lanthanide • Conductivity • Luminescence • Single-Molecule Magnet

[1]     G. Maurin, C. Serre, A. Cooper, G. Férey, *Chem. Soc. Rev.* **2017**, *46*, 3104–3107.
[2]     L. Sun, M. G. Campbell, M. Dincă, *Angew. Chem. Int. Ed.* **2016**, *55*, 3566–3579.
[3]     I. Stassen, N. Burtch, A. Talin, P. Falcaro, M. Allendorf, R. Ameloot, *Chem. Soc. Rev.* **2017**, *46*, 3185–3241.
[4]     G. Mínguez Espallargas, E. Coronado, *Chem. Soc. Rev.* **2018**, 533–557.
[5]     J. Rocha, L. D. Carlos, F. A. A. Paz, D. Ananias, *Chem. Soc. Rev.* **2011**, *40*, 926–940.
[6]     W. P. Lustig, S. Mukherjee, N. D. Rudd, A. V. Desai, J. Li, S. K. Ghosh, *Chem. Soc. Rev.* **2017**, *46*, 3242–3285.
[7]     B. Li, H. M. Wen, Y. Cui, W. Zhou, G. Qian, B. Chen, *Adv. Mater.* **2016**, *28*, 8819–8860.
[8]     H.-Y. Wang, L. Cui, J.-Z. Xie, C. F. Leong, D. M. D'Alessandro, J.-L. Zuo, *Coord. Chem. Rev.* **2017**, *345*, 342–361.
[9]     T. C. Narayan, T. Miyakai, S. Seki, M. Dincă, *J. Am. Chem. Soc.* **2012**, *134*, 12932–12935.
[10]     S. S. Park, E. R. Hontz, L. Sun, C. H. Hendon, A. Walsh, T. Van Voorhis, M. Dincă, *J. Am. Chem. Soc.* **2015**, *137*, 1774–1777.
[11]     H.-Y. Wang, J.-Y. Ge, C. Hua, C.-Q. Jiao, Y. Wu, C. F. Leong, D. M. D'Alessandro, T. Liu, J.-L. Zuo, *Angew. Chem. Int. Ed.* **2017**, *56*, 5465 –5470.
[12]     M. Souto, A. Santiago-Portillo, M. Palomino, I. J. Vitórica-Yrezábal, B. J. C. Vieira, J. C. Waerenborgh, S. Valencia, S. Navalón, F. Rey, H. García, G. Mínguez Espallargas, *Chem. Sci.* **2018**, *9*, 2413–2418.
[13]     J. Su, S. Yuan, H.-Y. Wang, L. Huang, J.-Y. Ge, E. Joseph, J. Qin, T. Cagin, J.-L. Zuo, H.-C. Zhou, *Nat. Commun.* **2017**, *8*, 2008.
[14]     M. Souto, J. Romero, J. Calbo, I. J. Vitorica-Yrezabal, J. L. Zafra, J. Casado Cordón, E. Ortí, A. Walsh, G. Mínguez Espallargas, *J. Am. Chem. Soc.* **2018**, *140*, 10562–10569.
[15]     D. M. P. Mingos, *Lanthanide Metal-Organic Frameworks*, Springer-Verlag Berlin Heidelberg, **2015**.
[16]     J. J. Baldoví, E. Coronado, A. Gaita-Ariño, C. Gamer, M. Giménez-Marqués, G. Mínguez Espallargas, *Chem. Eur. J.* **2014**, *20*, 10695–10702.
[17]     J. Castells-Gil, J. J. Baldoví, C. Martí-Gastaldo, G. Mínguez Espallargas, *Dalt. Trans.* **2018**, *47*, 14734–14740.
[18]     A. Gaita-Ariño, F. Luis, S. Hill, E. Coronado, *Nat. Chem.* **2019**, *11*, 301–309.
[19]     F. Pointillart, B. Le Guennic, S. Golhen, O. Cador, L. Ouahab, *Chem. Commun.* **2013**, *49*, 11632–11634.
[20]     F. Pointillart, B. Le Guennic, O. Cador, O. Maury, L. Ouahab, *Acc. Chem. Res.* **2015**, *48*, 2834–2842.
[21]     F. Pointillart, J. Jung, R. Berraud-pache, B. Le Guennic, V. Dorcet, O. Cador, O. Maury, Y. Guyot, S. Decurtins, S. Liu, et al., *Inorg. Chem.* **2015**, *54*, 5384–5397.
[22]     M. Bendikov, F. Wudl, D. F. Perepichka, *Chem. Rev.* **2004**, *104*, 4891–4945.
[23]     C. Rovira, *Chem. Rev.* **2004**, *104*, 5289–5317.
[24]     L. S. Xie, M. Dincă, *Isr. J. Chem.* **2018**, *2139*, 1119–1122.
[25]     J. Su, T. Hu, R. Murase, H. Wang, D. M. D. Alessandro, M. Kurmoo, J. Zuo, *Inorg. Chem.* **2019**, *58*, 3698–3706.
[26]     J. J. Baldoví, S. Cardona-Serra, J. M. Clemente-Juan, E. Coronado, A. Gaita-Ariño, A. Palii, *Inorg. Chem.* **2012**, *51*, 12565–12574.
[27]     Formula of **MUV-5a(Dy)** is $[Dy_3(TTFTB)_2(OOCCH_3)(OCHN(CH_3)_2]$ having a coordinated DMF instead of $H_2O$/OH since these crystals were not properly washed and activated by heating.
[28]     C. F. Macrae, P. R. Edgington, P. McCabe, E. Pidcock, G. P. Shields, R. Taylor, M. Towler, J. van de Streek, *J. Appl. Cryst.* **2006**, *39*, 453–457.
[29]     B. Chen, Z. P. Lv, C. F. Leong, Y. Zhao, D. M. D'alessandro, J. L. Zuo, *Cryst. Growth Des.* **2015**, *15*, 1861–1870.
[30]     B. Liu, B. Smit, *Langmuir* **2009**, *25*, 5918–5926.
[31]     T. J. Kistenmacher, T. E. Phillips, D. O. Cowan, *Acta Cryst.* **1974**, *B30*, 763–768.
[32]     V. Mukherjee, N. P. Singh, *Spectrochim Acta A Mol Biomol Spectrosc* **2014**, *117*, 315–322.
[33]     L. Sun, S. S. Park, D. Sheberla, M. Dincă, *J. Am. Chem. Soc.* **2016**, *138*, 14772–14782.
[34]     T. C. Umland, S. Allie, T. Kuhlmann, P. Coppens, *J. Phys. Chem.* **1988**, *92*, 6456–6460.
[35]     S. Vela, M. Souto, I. Ratera, C. Rovira, J. Veciana, *J. Phys. Chem. A* **2016**, *120*, 10297–10303.
[36]     M. J. Frisch, *Gaussian 09, Revision B.01, Gaussian, Inc., Wallingford CT,* **2016**.
[37]     A. D. Becke, *J. Chem. Phys.* **1993**, *98*, 5648–5652.
[38]     C. Adamo, V. Barone, *J. Chem. Phys.* **1999**, *110*, 6158–6170.
[39]     S. Abednatanzi, P. Gohari Derakhshandeh, H. Depauw, F.-X. Coudert, H. Vrielinck, P. Van Der Voort, K. Leus, *Chem. Soc. Rev.* **2019**, *48*, 2535–2565.
[40]     C. Strohhöofer, A. Polman, *Opt. Mater.* **2013**, *21*, 705–712.
[41]     K. A. White, D. A. Chengelis, K. A. Gogick, J. Stehman, N. L. Rosi, S. Petoud, *J. Am. Chem. Soc.* **2009**, *131*, 18069–18071.
[42]     F. Artizzu, F. Quochi, L. Marchiò, E. Sessini, M. Saba, A. Serpe, A. Mura, M. L. Mercuri, P. Bongiovanni, P. Deplano, *J. Phys. Chem. Lett.* **2013**, *4*, 3062–3066.
[43]     J. J. Baldoví, J. J. Borrás-Almenar, J. M. Clemente-Juan, E. Coronado, A. Gaita-Ariño, *Dalt. Trans.* **2012**, *41*, 13705–13710.
[44]     J. J. Baldoví, S. Cardona-Serra, J. M. Clemente-Juan, E. Coronado, A. Gaita-Ariño, A. Palii, *J. Comput. Chem.* **2013**, *34*, 1961–1967.
[45]     L. Escalera-Moreno, J. J. Baldoví, A. Gaita-Ariño, E. Coronado, *Chem. Sci.* **2018**, *9*, 3265–3275.

Supplementary Information

# Electronic, Structural and Functional Versatility in Tetrathiafulvalene-Lanthanide Metal-Organic Frameworks

Javier Castells-Gil,[a] Samuel Mañas-Valero,[a] Iñigo J. Vitórica-Yrezábal,[b] Duarte Ananias,[c] João Rocha,[c] Raul Santiago,[d] Stefan T. Bromley,[d,e] José J. Baldoví,[f] Eugenio Coronado,[a]  Manuel Souto*[a] and Guillermo Mínguez Espallargas*[a]

ᵃ Universidad de Valencia (ICMol), Catedrático José Beltrán 2, 46980, Paterna (Spain)
ᵇ School of Chemistry, University of Manchester Oxford Road, Manchester M13 9PL, United Kingdom
ᶜ Department of Chemistry and CICECO-Aveiro Institute of Materials University of Aveiro 3810-193 Aveiro, Portugal
ᵈ Departament de Ciència de Materials i Química Física & Institut de Química Teòrica i Computacional, Universitat de Barcelona, Universitat de Barcelona, C/Martí i Franquès 1, E-08028 Barcelona, Spain
ᵉ Institució Catalana de Recerca i Estudis Avançats (ICREA), E-08010 Barcelona, Spain
ᶠ Max Planck Institute for the Structure and Dynamics of Matter, Luruper Chaussee 149, D-22761 Hamburg, Germany

## Table of contents

## S1. Materials and reagents.

Ln(O$_2$CCH$_3$)$_3$·xH$_2$O precursors were purchased from Sigma-Aldrich and TCI Chemicals. *N,N*-dimethylformamide (DMF) (99.8%) and acetic acid (99.7%) were purchased from Sigma-Aldrich. Milli-Q water was used when required. All reagents and solvents were used as received without further purification.

## S2. Synthesis of materials and experimental details.

**Synthesis of MUV-5(Ln):** Common synthesis of **MUV-5** solids were carried out by suspending 16.5 µmol of Ln(CH$_3$COO)$_3$·xH$_2$O and 12.5 µmol of H$_4$TTFTB in a mixture of 1.3 mL of H$_2$O and 0.7 mL of AcOH (**MUV-5a**) or 1.5 mL of H$_2$O and 0.5 mL of AcOH (**MUV-5b**) in a 4 mL glass vial. The vial was sealed and sonicated for a few minutes to get a homogeneous suspension. The dark suspension was subsequently heated in an oven at 170 ºC for 12 hours (↑ +2.0 ºC min$^{-1}$, ↓ –0.4 ºC min$^{-1}$). After cooling down to room temperature, the dark red crystals were recovered by centrifugation and rinsed with fresh DMF, water and MeOH several times. The solid was then allowed to dry in air at room temperature, and was further heated at 150 ºC for at least 2 hours in order to yield activated **MUV-5a**. Anal. Elem. **MUV-5a** [Dy$_3$(C$_{34}$H$_{16}$O$_8$S$_4$)$_2$(OOCCH$_3$)(OCHN(CH$_3$)$_2$)]·(OCHN(CH$_3$)$_2$): Calcd.: C, 44.44; H, 2.40; S, 12.49; N, 1.36. Found: C, 45.33; H, 2.68; S, 12.37.; N, 0.99. **MUV-5b** [Dy(C$_{34}$H$_{16}$O$_8$S$_4$)(H$_2$O)](CH$_3$COOH]: Calcd.: C, 46.93; H, 2.41; S, 13.92. Found: C, 46.96; H, 2.67; S, 13.17.

## S3. Crystal data and structure refinement for MUV-5(Ln).

**Data Collection.** X-ray data for compounds **MUV-5a(Dy)** and **MUV-5a(Ho)** were collected at a temperature of 150 K using Rigaku FR-X with Cu-Kα radiation equipped with a HypixHE6000 detector. X-ray data for compounds **MUV-5a(Er)**, **MUV-5a(Gd)** and **MUV-5a(Tb)** were collected at a temperature of 100 K at I19 beamline at Diamond Light Source synchrotron.[1] X-ray data for compound **MUV-5b(Dy)** were collected at a temperature of 120 K using a Rigaku Supernova with Mo-Kα radiation equipped with an Eos CCD detector. All instruments were equipped with an Oxford Cryosystems nitrogen flow gas system. Data was measured using GDA for **MUV-5a(Er)** and **MUV-5a(Tb)** and CrysAlisPro suite of programs for MUV-5a(Dy), MUV-5a(Ho) and **MUV-5b(Dy)**.

**Crystal structure determinations and refinements.** X-ray data were processed and reduced using CrysAlisPro suite of programs. Absorption correction was performed using empirical methods (SCALE3 ABSPACK) based upon symmetry-equivalent reflections combined with measurements at different azimuthal angles.[2] The crystal structure was solved and refined against all $F^2$ values using the SHELXL and Olex 2 suite of programmes.[3,4]

All atoms in crystal structures were refined anisotropically with the exception of some water solvent molecules. Hydrogen atoms were placed in the calculated idealized positions for all compounds. Disordered water molecules and the hydrogen bond network produced suggest the possibility of having a disordered $H_2O$/OH (50/50) coordinated to the metal atoms in compounds MUV-5a(Ho), MUV-5a(Er), MUV-5a(Gd) and MUV-5a(Tb). All compounds present large voids filled with a lot of featureless electron density; solvent mask protocol implemented by Olex2 show the presence of 80 electrons approximately in the voids, which could correspond with 2 molecules of DMF per void.

CCDC 1934945-1934950 contains the supplementary crystallographic data for this paper. These data can be obtained free of charge *via* www.ccdc.cam.ac.uk/conts/retrieving.html (or from the Cambridge Crystallographic Data Centre, 12 Union Road, Cambridge CB21EZ, UK; fax: (+44)1223-336-033; or deposit@ccdc.cam.ac.uk).

**Table S1.** Crystallographic information for **MUV-5a(Dy)**, **MUV-5b(Dy)** and **MUV-5a(Er)**

| Identification code | MUV-5a(Dy) | MUV-5b(Dy) | MUV-5a(Er) |
|---|---|---|---|
| Empirical formula | $C_{73}H_{42}Dy_3NO_{19}S_8$ | $C_{36}H_{23}DyO_{11}S_4$ | $C_{70}H_{41.5}Er_3O_{21.5}S_8$ |
| Formula weight | 1981.05 | 922.28 | 1984.79 |
| Temperature/K | 150(2) | 120(2) | 100(2) |
| Crystal system | monoclinic | monoclinic | monoclinic |
| Space group | $P2/c$ | $P2_1/n$ | $P2/c$ |
| a/Å | 11.1878(9) | 20.8560(4) | 11.1440(2) |
| b/Å | 11.0780(9) | 10.30930(10) | 11.3378(2) |
| c/Å | 32.841(2) | 21.1597(4) | 32.2847(4) |
| α/° | 90 | 90 | 90.0 |
| β/° | 91.771(7) | 116.201(2) | 91.3192(14) |
| γ/° | 90 | 90 | 90 |
| Volume/Å³ | 4068.3(6) | 4082.10(13) | 4078.04(11) |
| Z | 2 | 4 | 2 |
| $\rho_{calc}$g/cm³ | 1.617 | 1.501 | 1.616 |
| μ/mm⁻¹ | 16.980 | 2.089 | 3.325 |
| F(000) | 1930.0 | 1828.0 | 1931.0 |
| Crystal size/mm³ | $0.03 \times 0.012 \times 0.01$ | $0.18 \times 0.04 \times 0.01$ | $0.018 \times 0.01 \times 0.01$ |
| Radiation | CuKα (λ = 1.54184) | MoKα (λ = 0.71073) | synchrotron (λ = 0.6889) |
| 2Θ range for data collection/° | 5.384 to 133.194 | 6.854 to 56.204 | 3.482 to 49.038 |
| Index ranges | $-13 \leq h \leq 12, -11 \leq k \leq 13, -38 \leq l \leq 39$ | $-27 \leq h \leq 26, -13 \leq k \leq 13, -26 \leq l \leq 27$ | $-13 \leq h \leq 12, -13 \leq k \leq 12, -38 \leq l \leq 38$ |
| Reflections collected | 22453 | 45547 | 27237 |
| Independent reflections | 6883 [$R_{int}$ = 0.0771, $R_{sigma}$ = 0.0681] | 9020 [$R_{int}$ = 0.0678, $R_{sigma}$ = 0.0665] | 7066 [$R_{int}$ = 0.0632, $R_{sigma}$ = 0.0794] |
| Data/restraints/parameters | 6883/32/515 | 9020/11/491 | 7066/0/489 |
| Goodness-of-fit on F² | 1.098 | 1.038 | 1.077 |
| Final R indexes [I>=2σ (I)] | $R_1$ = 0.0795, $wR_2$ = 0.2159 | $R_1$ = 0.0407, $wR_2$ = 0.0715 | $R_1$ = 0.0528, $wR_2$ = 0.1412 |
| Final R indexes [all data] | $R_1$ = 0.1044, $wR_2$ = 0.2335 | $R_1$ = 0.0561, $wR_2$ = 0.0757 | $R_1$ = 0.0546, $wR_2$ = 0.1424 |
| Largest diff. peak/hole / e Å⁻³ | 2.03/-1.74 | 0.89/-0.80 | 2.23/-1.99 |

**Table S2.** Crystallographic information for **MUV-5a(Gd)**, **MUV-5a(Ho)** and **MUV-5a(Tb)**

| Identification code | MUV-5a(Gd) | MUV-5a(Ho) | MUV-5a(Tb) |
|---|---|---|---|
| Empirical formula | $C_{70}H_{41.5}Gd_3O_{21.5}S_8$ | $C_{70}H_{41.5}Ho_3O_{21.5}S_8$ | $C_{70}H_{41.5}O_{21.5}S_8Tb_3$ |
| Formula weight | 1954.76 | 1977.80 | 1959.77 |
| Temperature/K | 100(2) | 150(2) | 100(2) |
| Crystal system | monoclinic | monoclinic | monoclinic |
| Space group | $P2/c$ | $P2/c$ | $P2/c$ |
| a/Å | 11.2561(4) | 11.1706(2) | 11.2108(3) |
| b/Å | 11.3522(3) | 11.35300(10) | 11.2909(4) |
| c/Å | 32.2895(8) | 32.3407(4) | 32.4084(9) |
| α/° | 90 | 90 | 90 |
| β/° | 91.534(3) | 91.6000(10) | 91.719(2) |
| γ/° | 90 | 90 | 90 |
| Volume/Å$^3$ | 4124.5(2) | 4099.84(10) | 4100.4(2) |
| Z | 2 | 2 | 2 |
| $\rho_{calc}$g/cm$^3$ | 1.574 | 1.602 | 1.587 |
| μ/mm$^{-1}$ | 2.647 | 7.645 | 2.807 |
| F(000) | 1907.0 | 1925.0 | 1913.0 |
| Crystal size/mm$^3$ | $0.12 \times 0.02 \times 0.02$ | $0.22 \times 0.12 \times 0.1$ | $0.07 \times 0.01 \times 0.01$ |
| Radiation | synchrotron (λ = 0.6889) | CuKα (λ = 1.54184) | synchrotron (λ = 0.6889) |
| 2Θ range for data collection/° | 2.446 to 49.036 | 7.918 to 152.876 | 3.496 to 49.038 |
| Index ranges | -12 ≤ h ≤ 13, -13 ≤ k ≤ 13, -38 ≤ l ≤ 37 | -12 ≤ h ≤ 13, -14 ≤ k ≤ 13, -40 ≤ l ≤ 40 | -13 ≤ h ≤ 13, -13 ≤ k ≤ 13, -39 ≤ l ≤ 39 |
| Reflections collected | 27365 | 125974 | 49332 |
| Independent reflections | 7311 [$R_{int}$ = 0.1772, $R_{sigma}$ = 0.1912] | 8424 [$R_{int}$ = 0.0478, $R_{sigma}$ = 0.0156] | 7505 [$R_{int}$ = 0.0921, $R_{sigma}$ = 0.0581] |
| Data/restraints/parameters | 7311/0/484 | 8424/30/498 | 7505/30/493 |
| Goodness-of-fit on F$^2$ | 1.057 | 1.104 | 1.060 |
| Final R indexes [I>=2σ (I)] | $R_1$ = 0.1124, w$R_2$ = 0.2983 | $R_1$ = 0.0721, w$R_2$ = 0.1526 | $R_1$ = 0.0642, w$R_2$ = 0.1672 |
| Final R indexes [all data] | $R_1$ = 0.1230, w$R_2$ = 0.3120 | $R_1$ = 0.0724, w$R_2$ = 0.1528 | $R_1$ = 0.0717, w$R_2$ = 0.1720 |
| Largest diff. peak/hole / e Å$^{-3}$ | 3.07/-1.29 | 1.58/-1.93 | 2.95/-1.57 |
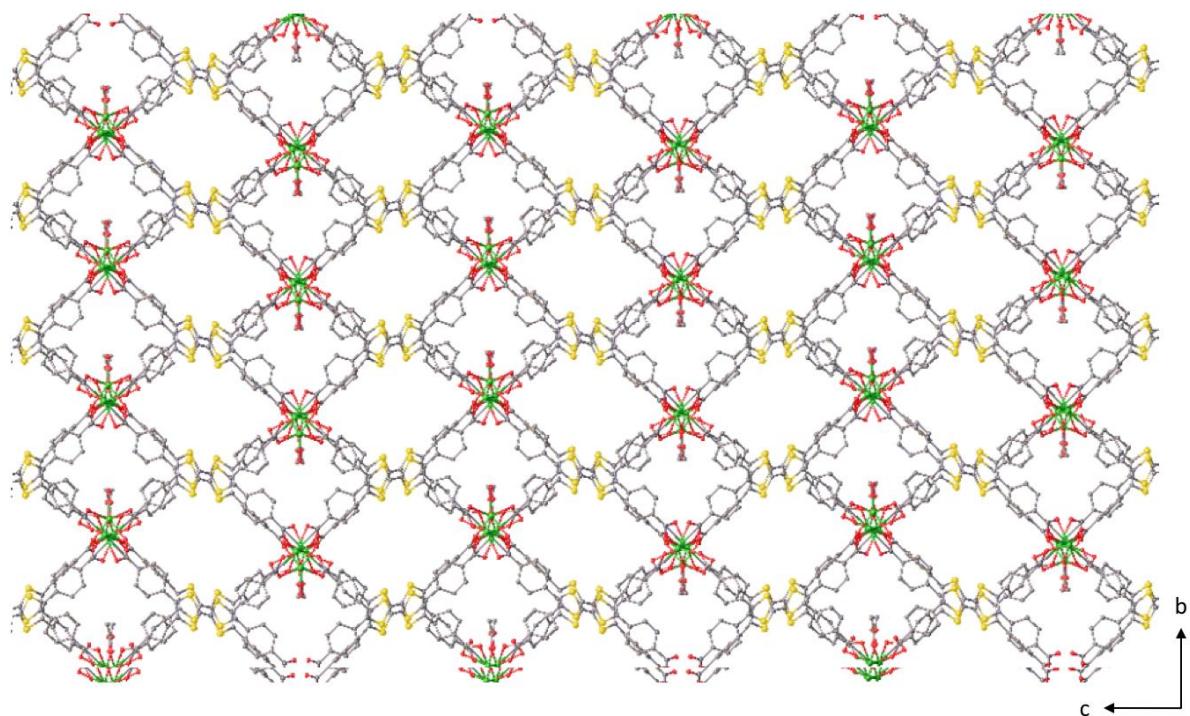
**Figure S1.** View of the structure of **MUV-5a** along the *a*-axis. Colour code: C (grey), O (red), Ln (green), S (yellow).
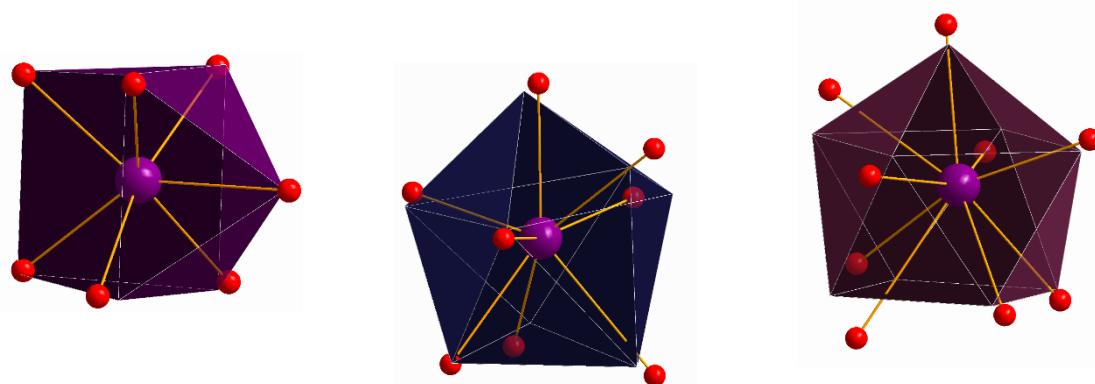


**Figure S2**. Coordination geometry of the Ln ions in **MUV-5a**: 7-coordinated Ln (*left*), 8-coordinated Ln (*middle*) and 9-coordinated Ln (*right*).
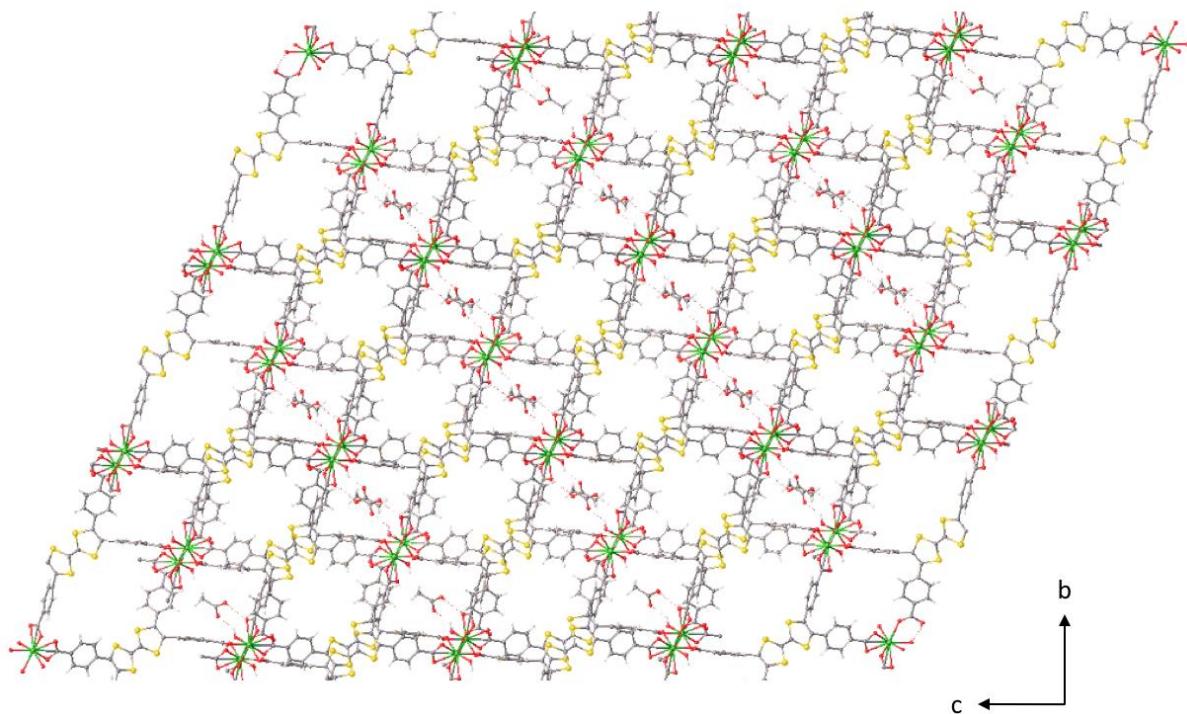
**Figure S3.** View of the structure of **MUV-5b** along the *a*-axis. Colour code: C (grey), O (red), Ln (green), S (yellow).
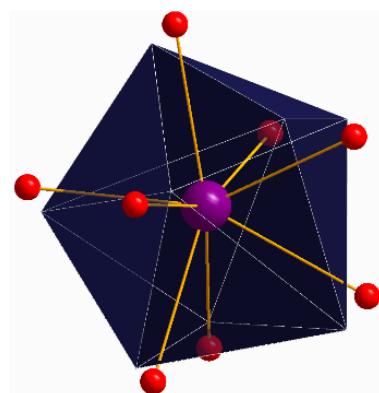


**Figure S4**. Coordination geometry of the 8-coordinated Ln(III) ions in **MUV-5b**

**MUV-5a(Dy)**　　　　　　　**MUV-5b(Dy)**



4.03 Å

3.67 Å

5.92 Å

4.88 Å
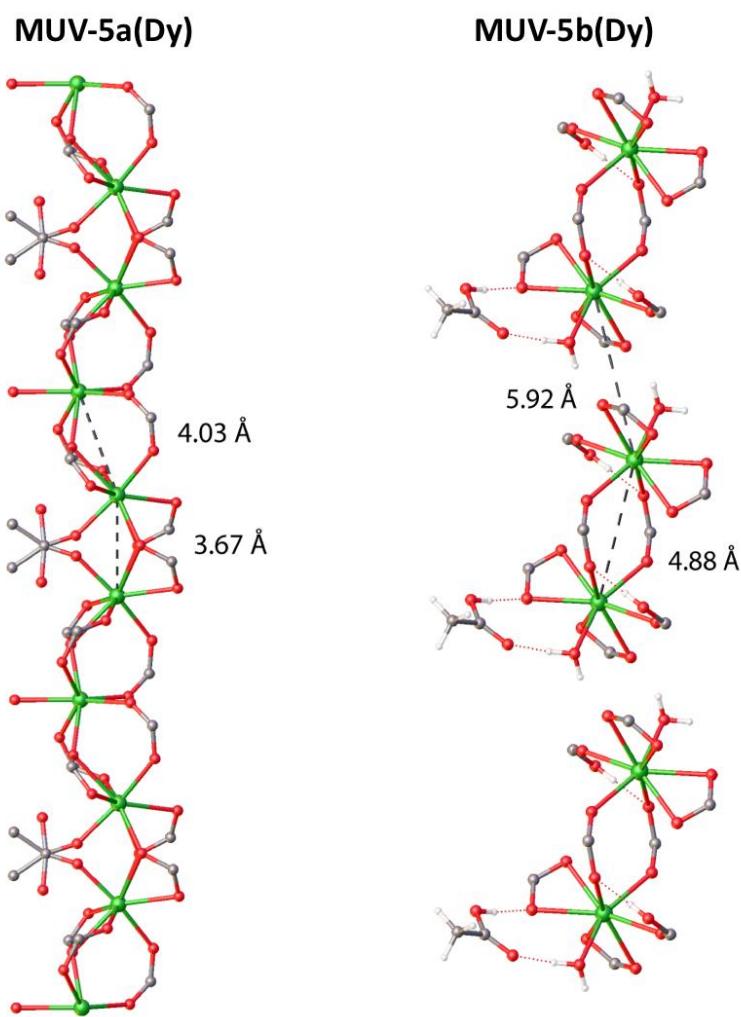
**Figure S5**. Comparison between the Ln-carboxylate chain found in **MUV-5a(Dy)** (left) and the discrete Ln$_2$ SBU present in **MUV-5b(Dy)** (right). Colour code: C (grey), O (red), Ln (green), H (white). The dashed lines show the distances between Ln pairs.

MUV-5a(Dy)　　　　　　　MUV-5b(Dy)



5°

17°
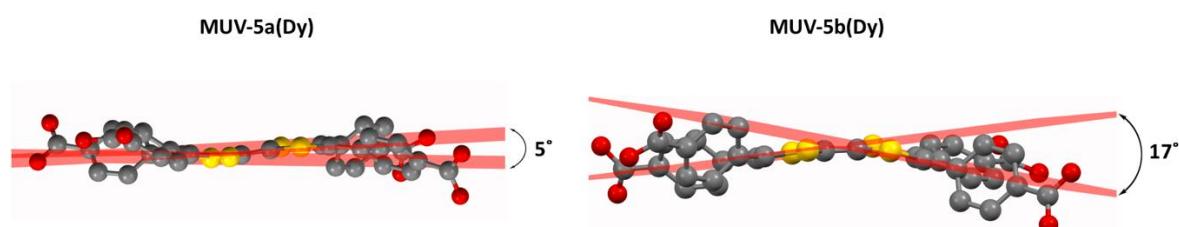
**Figure S6**. Calculated dihedral angles for **MUV-5a(Dy)** and **MUV-5b(Dy).**

## S4. Chemical Characterization

**Powder X-Ray Diffraction (PXRD)**

Powder XRD patterns were collected for polycrystalline samples using a 0.5 mm borosilicate capillary mounted and aligned in a PANalytical Empyrean diffractometer using copper radiation (Cu K$\alpha$ $\lambda$ = 1.5418 Å) with an PIXcel detector, operating at 40 mA and 45 kV. Profiles for refinement were collected by using a Soller Slit of 0.02º and a divergence slit of ¼ at room temperature in the angular range 3° < 2θ < 40° with a step size of 0.013°. LeBail refinements were carried out with the FULLPROF software package.
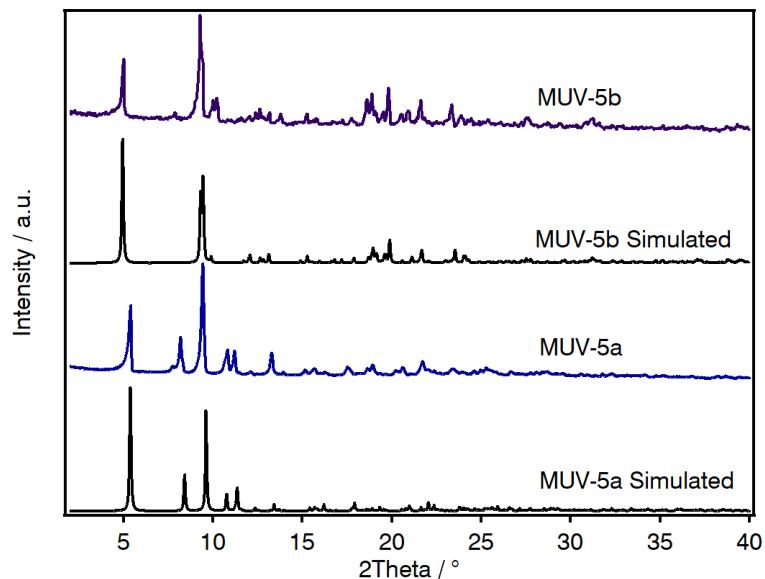


**Figure S7**. PXRD of simulated and experimental **MUV-5a(Dy)** and **MUV-5b(Dy)**.
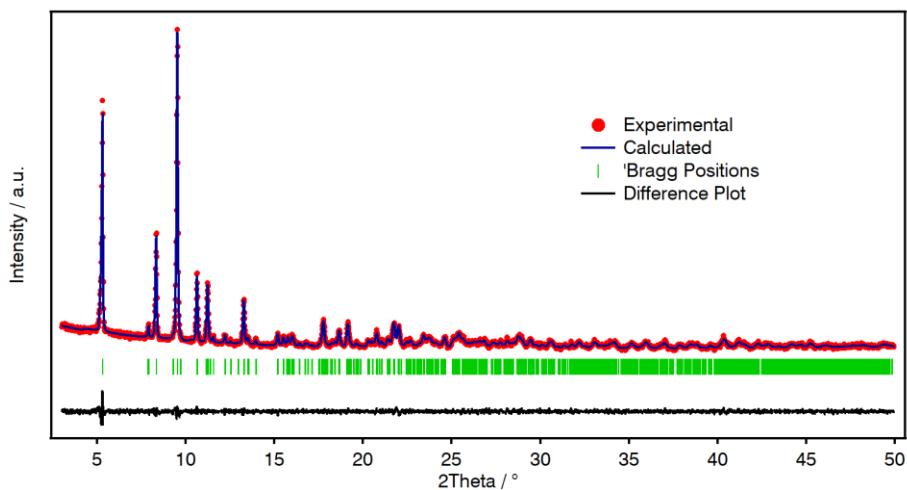


**Figure S8**. Experimental (red dots), calculated (blue line), difference plot [$(I_{obs}-I_{calc})$] (black line) and Bragg positions (green ticks) for the LeBail refinement of experimental diffraction data of **MUV-5a(Dy)** collected at room temperature by using single-crystal data from **MUV-5a(Dy)** as starting parameters

**Table S3**. Summary of the parameters obtained from LeBail refinement. Note that the differences observed can be attributed to the different experimental temperatures.

| Compound | $a$ [Å] | $b$ [Å] | $c$ [Å] | $\beta$ [°] | $V$ [Å$^3$] | $R_e$ [%] | $R_p$ [%] | $R_{wp}$ [%] | gof |
|---|---|---|---|---|---|---|---|---|---|
| **MUV-5a(Dy)** | 11.247 | 11.168 | 33.254 | 92.67 | 4172 | 4.92 | 4.36 | 5.58 | 1.1 |
| **MUV-5a(Dy) Single crystal** | 11.188 | 11.078 | 32.841 | 91.771 | 4068 | - | - | - | - |
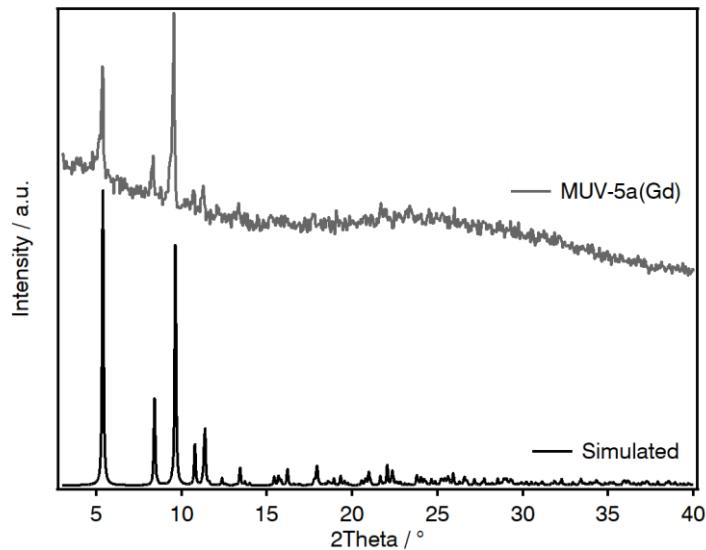


**Figure S9**. Experimental (grey) and simulated (black) PXRD of **MUV-5a(Gd).**
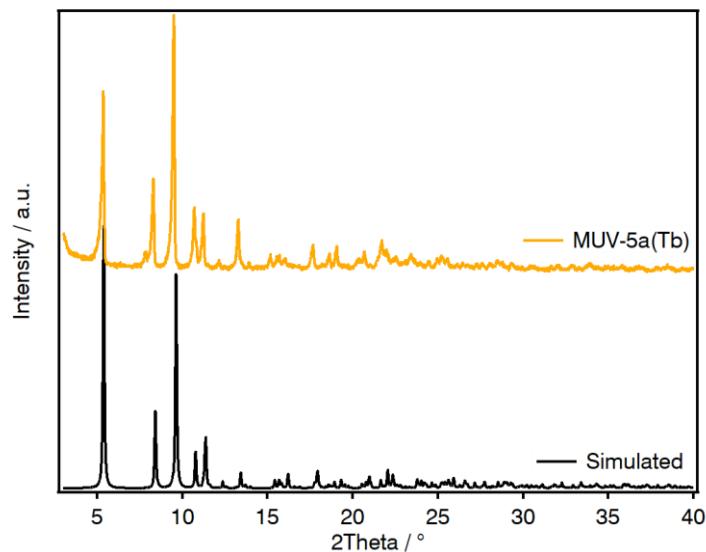


**Figure S10**. Experimental (yellow) and simulated (black) PXRD of **MUV-5a(Tb).**
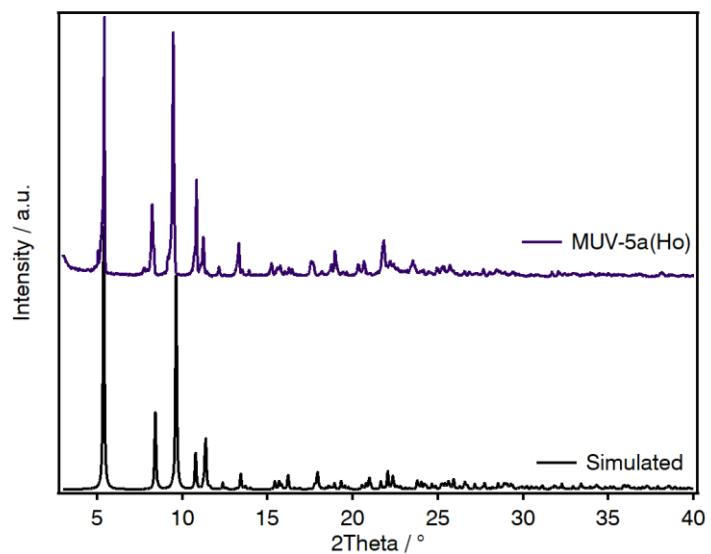
**Figure S11**. Experimental (purple) and simulated (black) PXRD of **MUV-5a(Ho).**
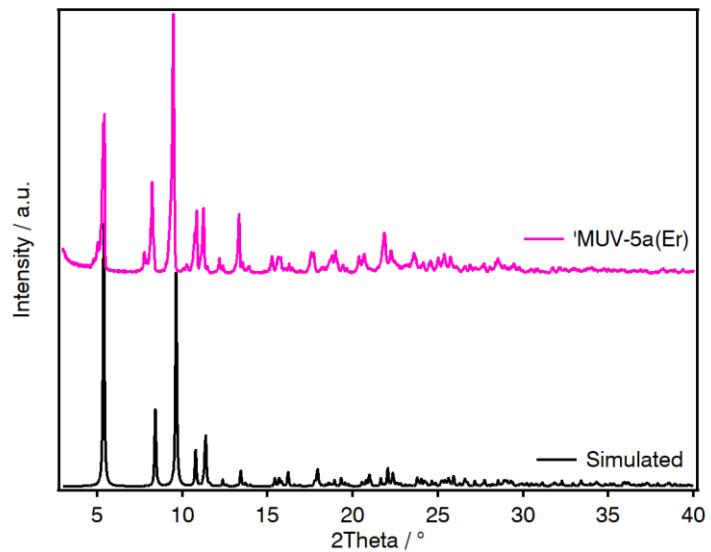


**Figure S12**. Experimental (pink) and simulated (black) PXRD of **MUV-5a(Er).**

**Thermogravimetric Analysis (TG-SDTA)**

TGA-SDTA curves were recorded at a ramp rate of 5 ºC/min on a Mettler Toledo TGA/SDTA 851e/SF/1100 apparatus between 25 and 700 ℃ under synthetic air.
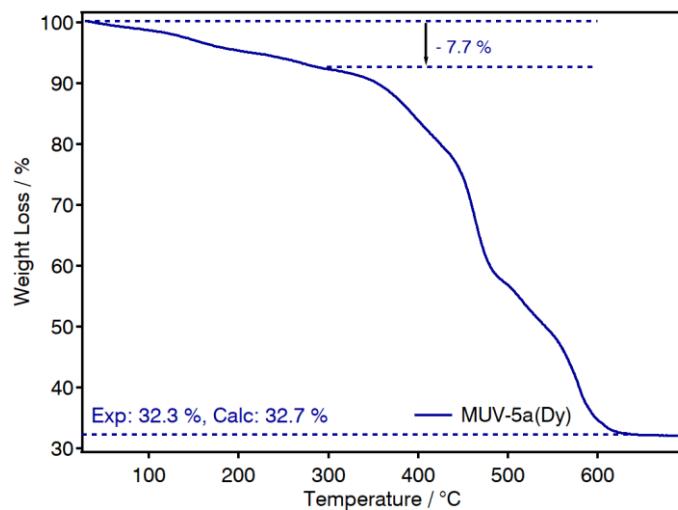


**Figure S13**. Thermogravimetric analysis of **MUV-5a(Dy)** in air. The first weight loss corresponds to the departure of DMF molecules (-2 · $(CH_3)_2NCHO$; Exp.: 7.7 %; Calcd.: 7.5 %).
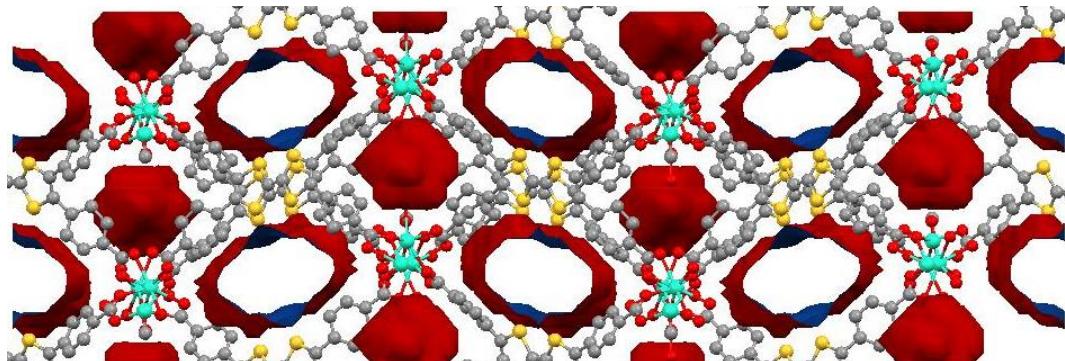


**Figure S14**. Representation of the void volume of **MUV-5a** as calculated by Mercury.

## Gas adsorption/desorption isotherms

Gas adsorption measurements were recorded ex situ on **MUV-5a** solids on a Micromeritics 3Flex apparatus. Samples were degassed overnight at 150 ℃ and $10^{-6}$ Torr prior to analysis. High-pressure gas sorption studies (up to 12 bar) were performed in a gravimetric sorption analyser IGA-100 (Hiden Isochema). The sample was degassed 2 hours at 150 ℃ under vacuum. $CO_2$ adsorption isotherms were acquired at 10, 25, 40 and 60 ℃.
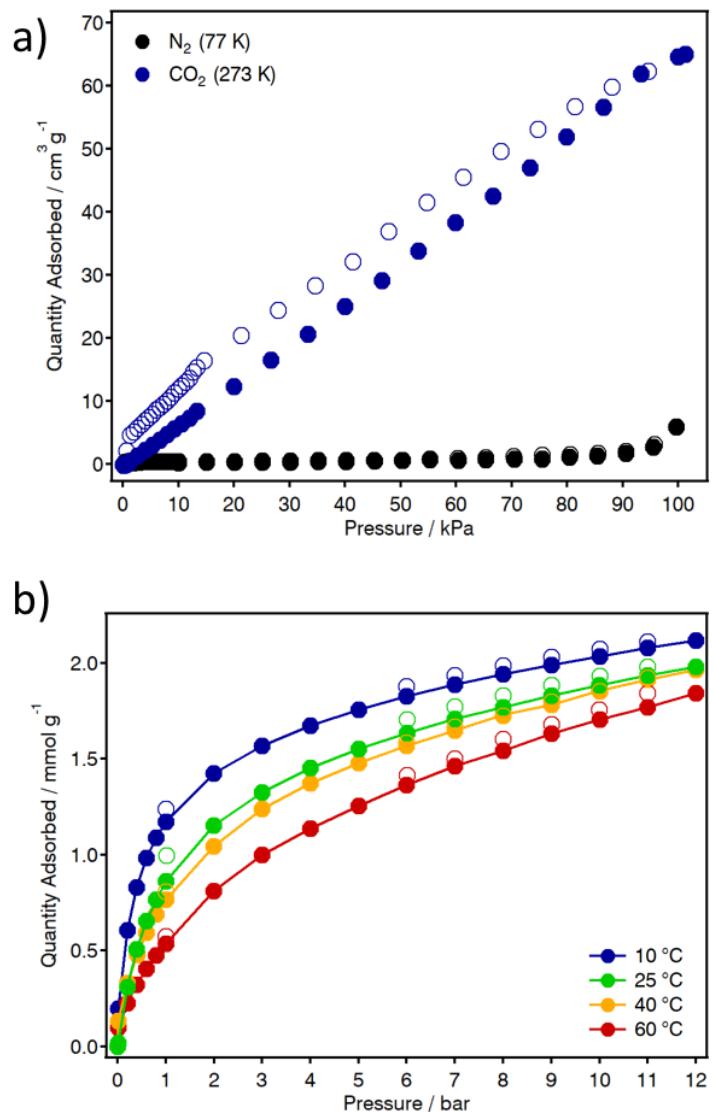


**Figure S15**. a) $N_2$ (black) and $CO_2$ (blue) volumetric adsorption-desorption isotherms of **MUV-5a(Dy)** performed at 77 and 273 K, respectively. Filled and open symbols represent the adsorption and the desorption branch, respectively. b) Gravimetric adsorption (closed symbols) and desorption (open symbols) isotherms of $CO_2$ at different temperatures in **MUV-5a(Dy)**.

**Electron Paramagnetic Resonance (EPR)**

EPR measurements were performed on approximately 3 mg of solid. EPR data was recorded in a Bruker ELEXYS E580 spectrometer under X-band irradiation (~ 9.3 GHz) at room temperature.
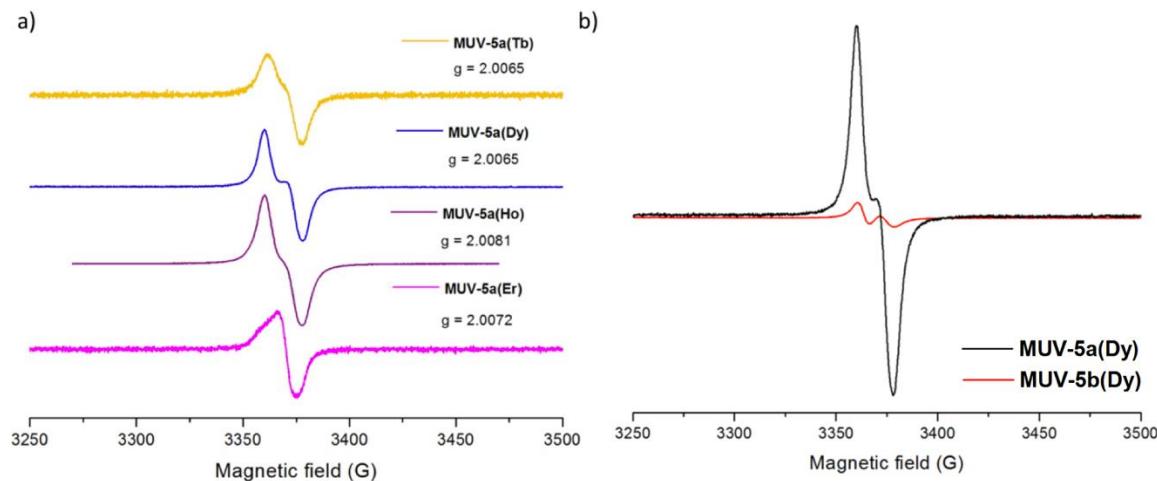


**Figure S16**. a) EPR spectra of **MUV-5a(Ln)** recorded at room temperature. b) Comparison of EPR intensities for **MUV-5a(Dy)** and **MUV-5b(Dy)** at room temperature.

**Scanning Electron Microscope (SEM)**
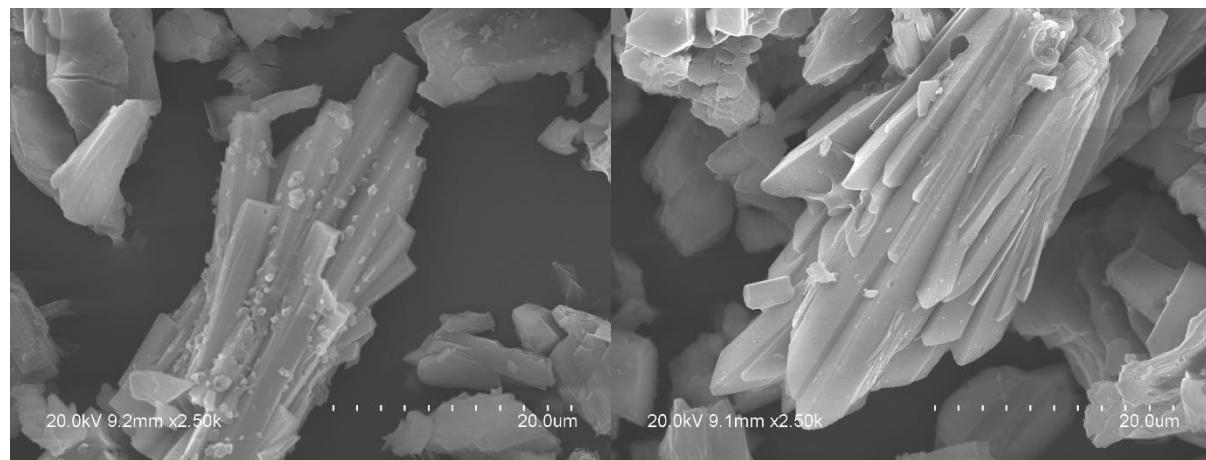


**Figure S17**. Scanning Electron Microscopy (SEM) images of **MUV-5a(Dy)**.

## S5. Electrical Measurements

Powders of **MUV-5** were pressed to form pellets (P ≈ 5 US tons), cut with rectangular shapes and contacted with platinum wires (Goodfellow, 99.99%, 25 μm of diameter) and silver conductive paint (RS 123-9911) in a 4 probe configuration (Figures S18-S29). The geometrical factors (width, length and thickness) were measured using an optical microscope (width and length were determined from the top view, Figures S18-26a, and the thickness from the lateral one, Figures S18-29b). I-V curves were measured with a Keithley 2450 sourcemeter, applying a current bias through the external leads and measuring the voltage drop by the internal ones. The conductivity ($\sigma = \frac{1}{R} \cdot \frac{l}{w \cdot t}$, where R is the resistance, l is the length between the leads, w is the width of the sample and t its thickness) was obtained taking into account the geometrical factors and the resistance obtained by fitting the ohmic regime of the I-V curves (Figures S18-29c).

Typical samples and an I-V curve at room temperature is shown in Figures S18 - S29. The values obtained for the different **MUV-5** samples are summarized in the Table S4.

**Table S4**. Geometrical factors (length, l, width, w, and thickness, t), resistance obtained by the linear fit of the ohmic regime of the I-V curves and conductivity at 300 K for the different **MUV-5** systems.

| MUV-5a | l (μm) | w (μm) | t (μm) | R (Ω) at 300 K | σ (S/cm) at 300 K |
|---|---|---|---|---|---|
| **Dy#1** | 130 | 370 | 90 | $(8.35 \pm 0.016) \cdot 10^{7}$ | $4.68 \cdot 10^{-7}$ |
| **Dy#2** | 190 | 335 | 210 | $(1.41 \pm 0.03) \cdot 10^{8}$ | $1.92 \cdot 10^{-7}$ |
| **Gd#1** | 185 | 430 | 130 | $(1.032 \pm 0.16) \cdot 10^{8}$ | $3.21 \cdot 10^{-7}$ |
| **Gd#2** | 320 | 370 | 200 | $(5.49 \pm 0.05) \cdot 10^{8}$ | $7.87 \cdot 10^{-8}$ |
| **Tb#1** | 245 | 320 | 105 | $(9.34 \pm 0.04) \cdot 10^{6}$ | $7.81 \cdot 10^{-6}$ |
| **Tb#2** | 340 | 680 | 85 | $(2.75 \pm 0.02) \cdot 10^{6}$ | $2.13 \cdot 10^{-5}$ |
| **Ho#1** | 290 | 635 | 405 | $(3.604 \pm 0.005) \cdot 10^{6}$ | $3.12 \cdot 10^{-6}$ |
| **Ho#2** | 240 | 615 | 145 | $(2.602 \pm 0.002) \cdot 10^{6}$ | $1.03 \cdot 10^{-5}$ |
| **Er#1** | 375 | 580 | 160 | $(3.347 \pm 0.016) \cdot 10^{6}$ | $1.21 \cdot 10^{-5}$ |
| **Er#2** | 270 | 660 | 215 | $(7.0164 \pm 0.0008) \cdot 10^{6}$ | $2.71 \cdot 10^{-6}$ |
| MUV-5b | l (μm) | w (μm) | t (μm) | R (Ω) at 300 K | σ (S/cm) at 300 K |
| **Dy#1** | 370 | 590 | 150 | $(1.214 \pm 0.004) \cdot 10^{9}$ | $3.43 \cdot 10^{-8}$ |
| **Dy#1** | 230 | 400 | 170 | $(1.0466 \pm 0.0019) \cdot 10^{9}$ | $3.23 \cdot 10^{-8}$ |

a



250 μm

b

250 μm

c
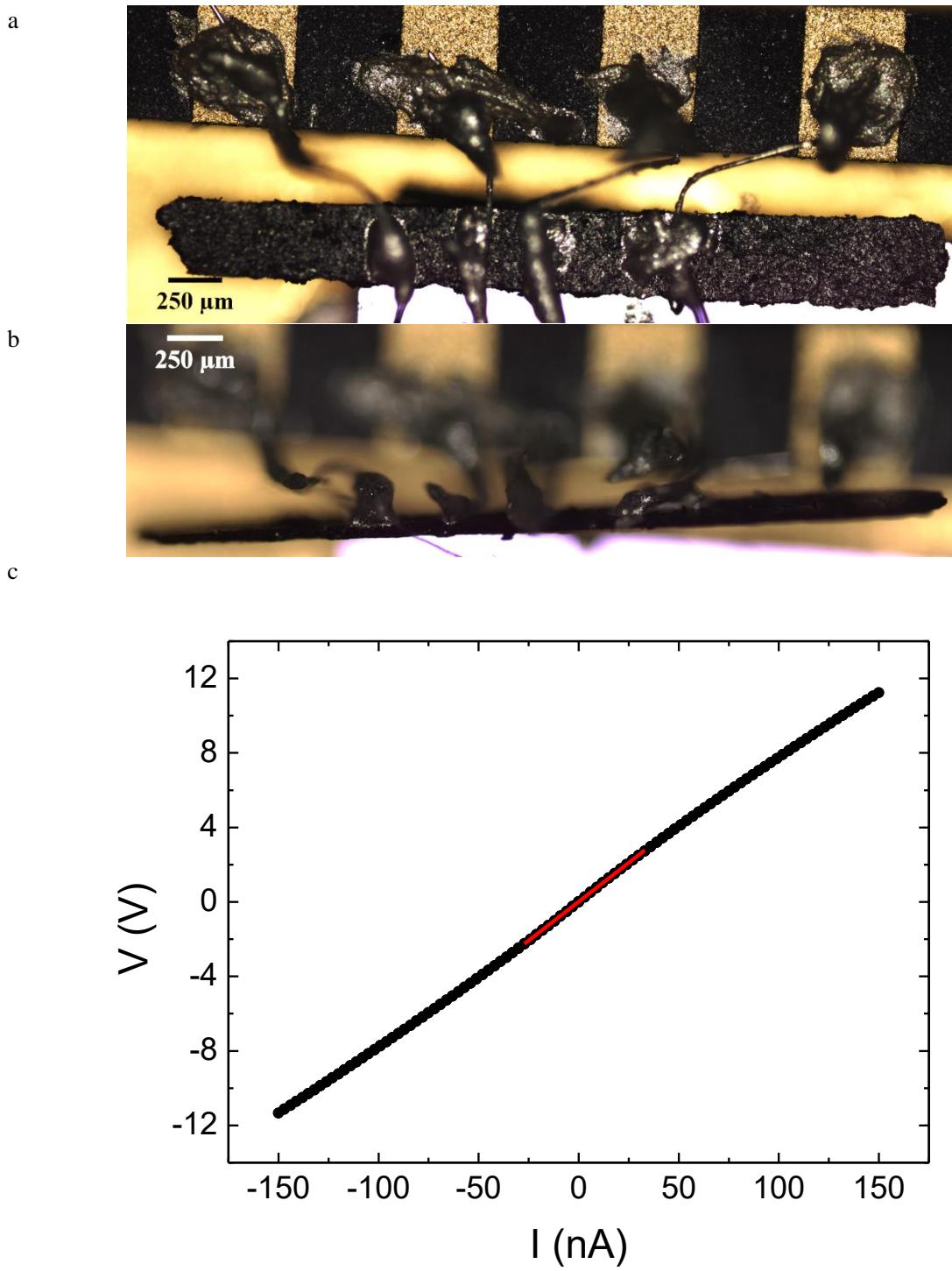


**Figure S18**. Device and electrical response of **MUV-5a(Dy)**#1. a) Top view. b) Lateral view. c) I-V curve at 300 K with the corresponding linear fit (red) of the ohmic regime. The fit gives as a result a slope of $(8.35 \pm 0.016) \cdot 10^7$ $\Omega$ and a y-intercept value of $(0.012 \pm 0.003)$ V, with $R^2 = 0.99992$.
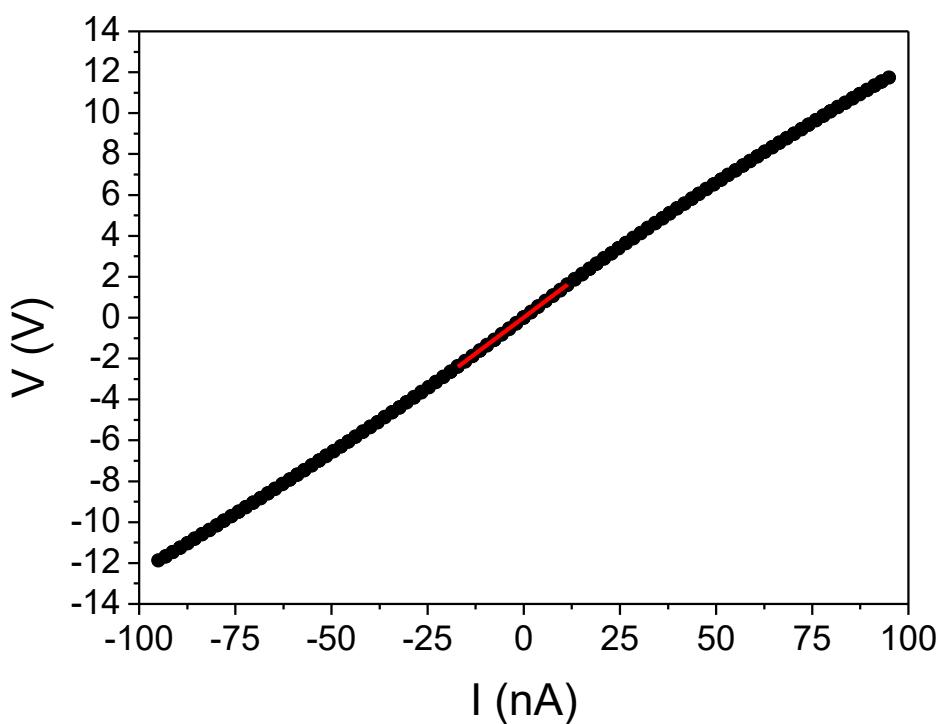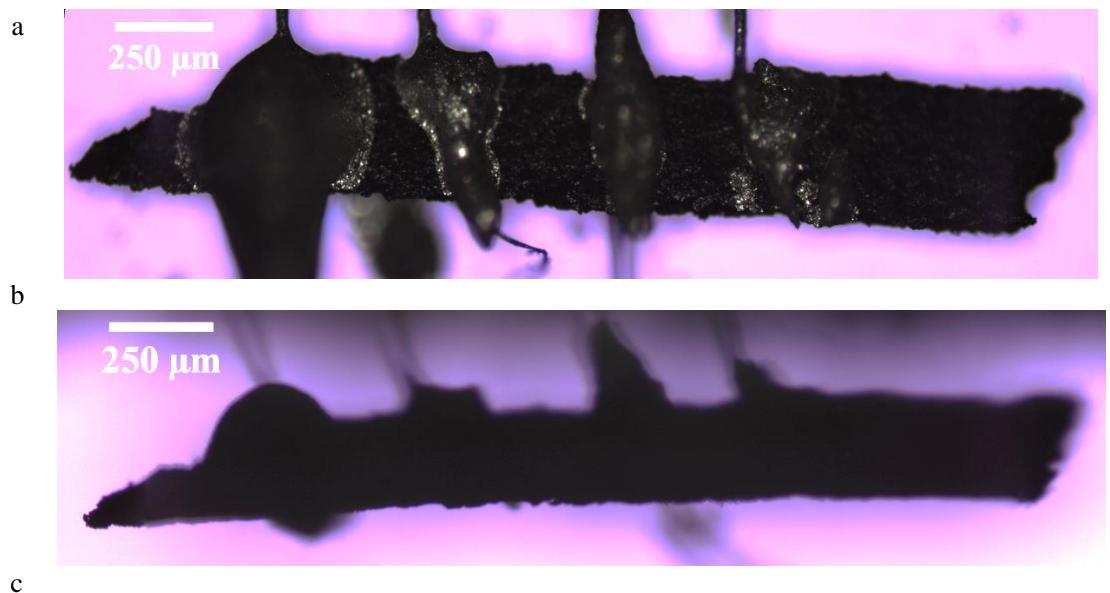
**Figure S19**. Device and electrical response of **MUV-5a(Dy)**#2. a) Top view. b) Lateral view. c) I-V curve at 300 K with the corresponding linear fit (red) of the ohmic regime. The fit gives as a result a slope of $(1.41 \pm 0.03) \cdot 10^8 \ \Omega$ and a y-intercept value of $(0.011 \pm 0.003)$ V, with $R^2 = 0.99994$.

a



b
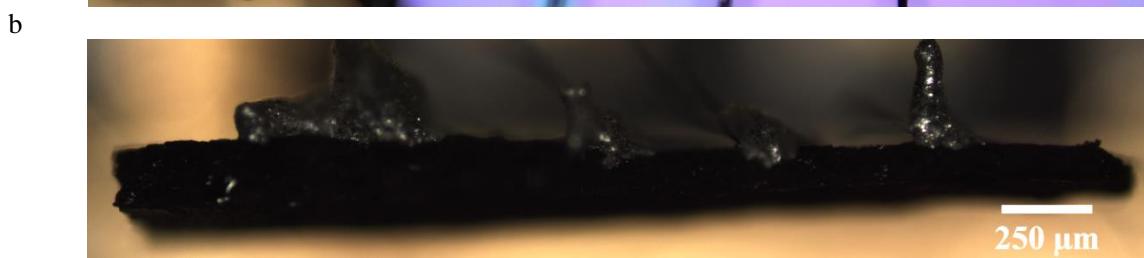


c
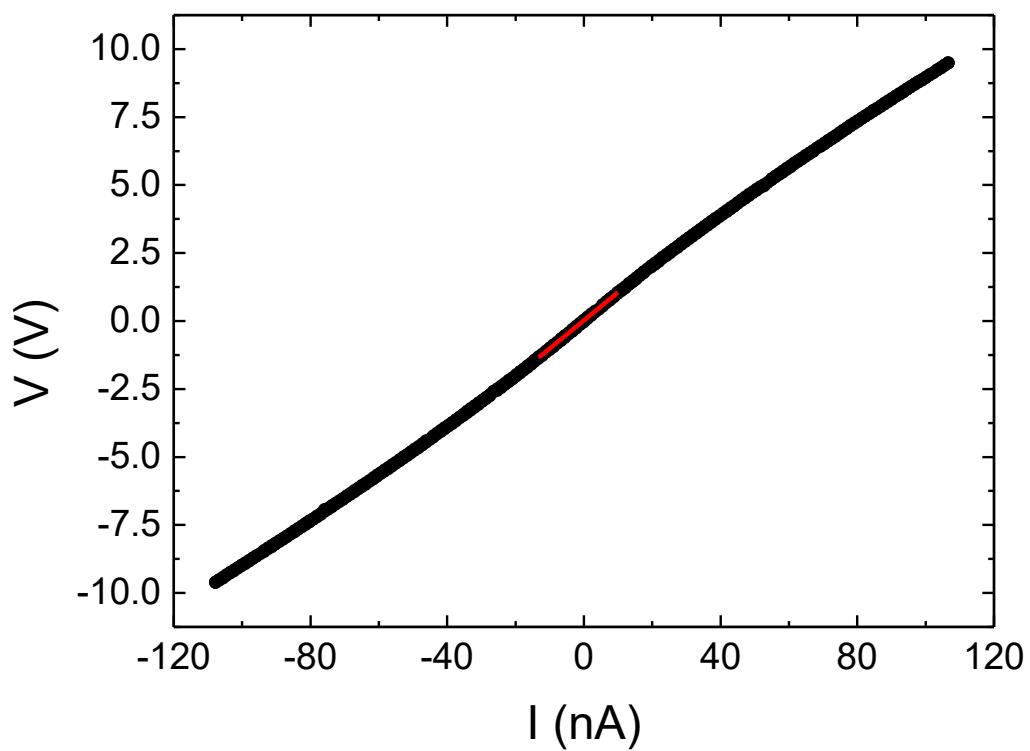


**Figure S20**. Device and electrical response of **MUV-5a(Gd)**#1. a) Top view. b) Lateral view. c) I-V curve at 300 K with the corresponding linear fit (red) of the ohmic regime. The fit gives as a result a slope of $(1.032 \pm 0.16) \cdot 10^8$ $\Omega$ and a y-intercept value of $(0.0216 \pm 0.0012)$ V, with $R^2 = 0.99995$.

a



b



c
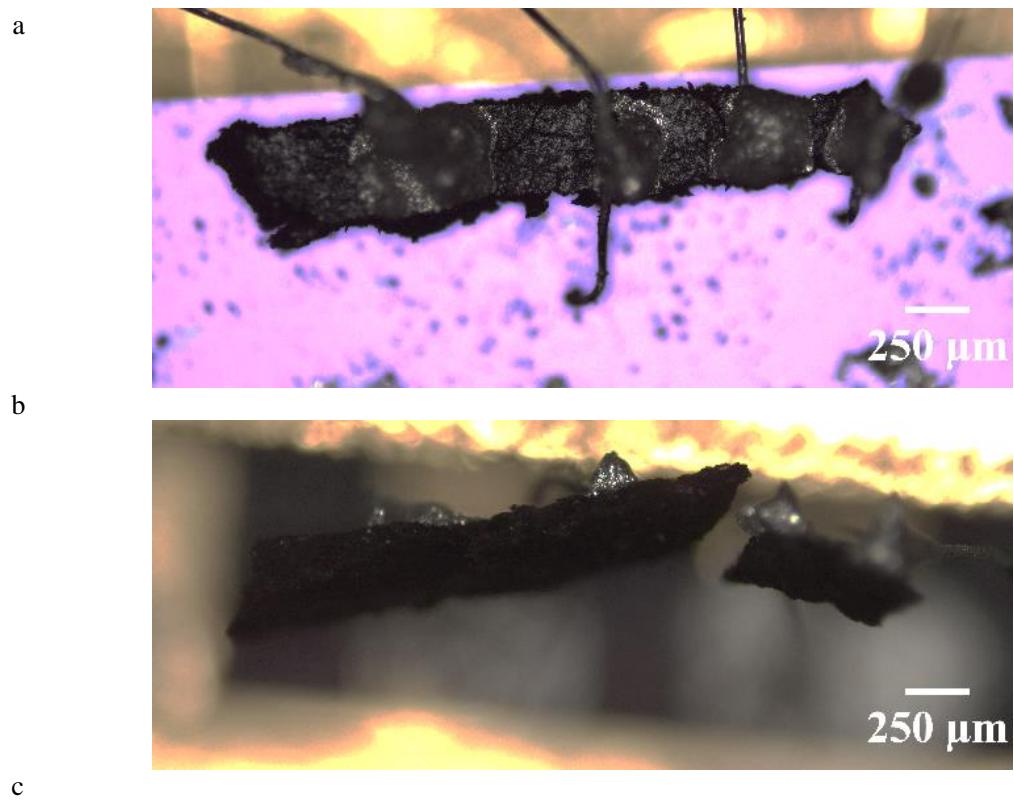


**Figure S21**. Device and electrical response of **MUV-5a(Gd)**#2. a) Top view. b) Lateral view. c) I-V curve at 300 K with the corresponding linear fit (red) of the ohmic regime. The fit gives as a result a slope of $(5.49 \pm 0.05) \cdot 10^8$ $\Omega$ and a y-intercept value of $(0.034 \pm 0.008)$ V, with $R^2 = 0.9994$.
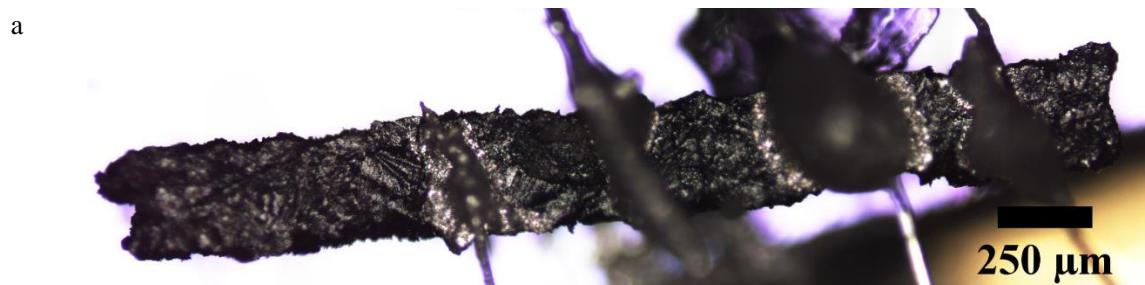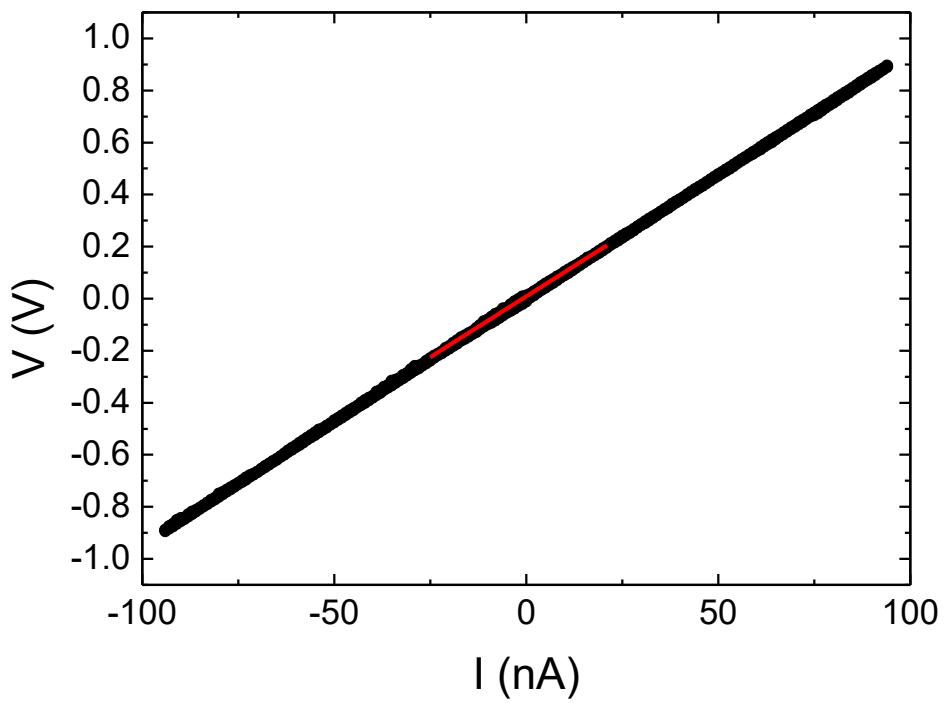
**Figure S22**. Device and electrical response of **MUV-5a(Tb)**#1. a) Top view. b) Lateral view. c) I-V curve at 300 K with the corresponding linear fit (red) of the ohmic regime. The fit gives as a result a slope of $(9.34 \pm 0.04) \cdot 10^6$ $\Omega$ and a y-intercept value of $(0.0086 \pm 0.0006)$ V, with $R^2 = 0.99902$.

a



b
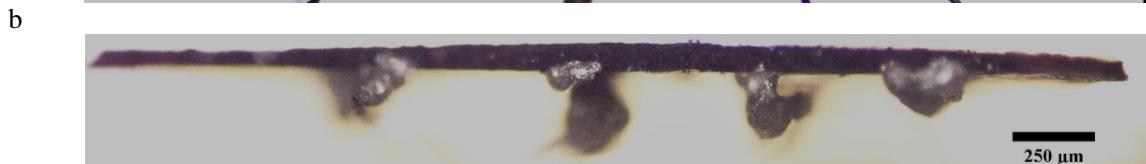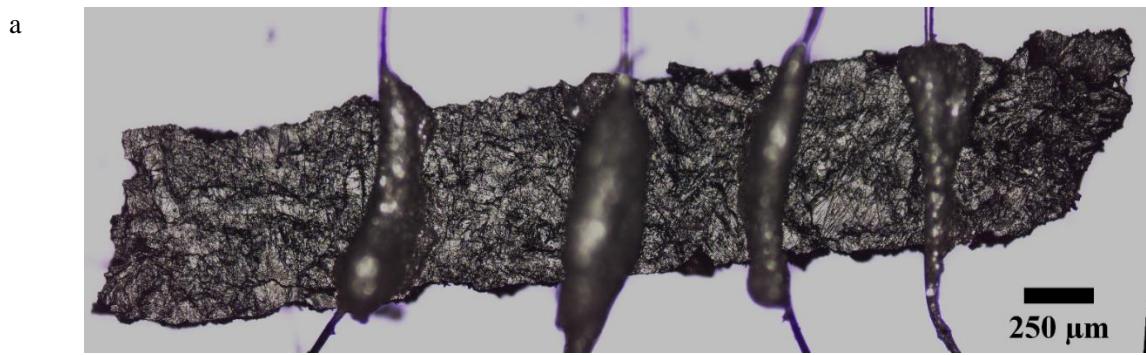


c
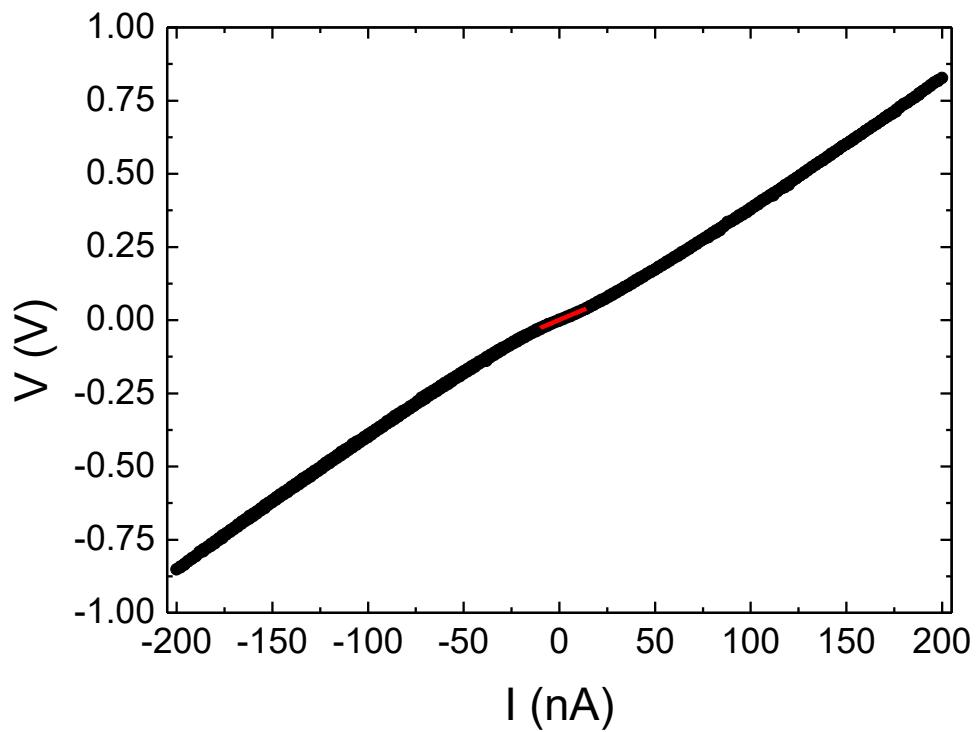


**Figure S23**. Device and electrical response of **MUV-5a(Tb)**#2. a) Top view. b) Lateral view. c) I-V curve at 300 K with the corresponding linear fit (red) of the ohmic regime. The fit gives as a result a slope of $(2.75 \pm 0.02) \cdot 10^6$ $\Omega$ and a y-intercept value of $(0.00081 \pm 0.00018)$ V, with $R^2 = 0.99913$.

a



b



c
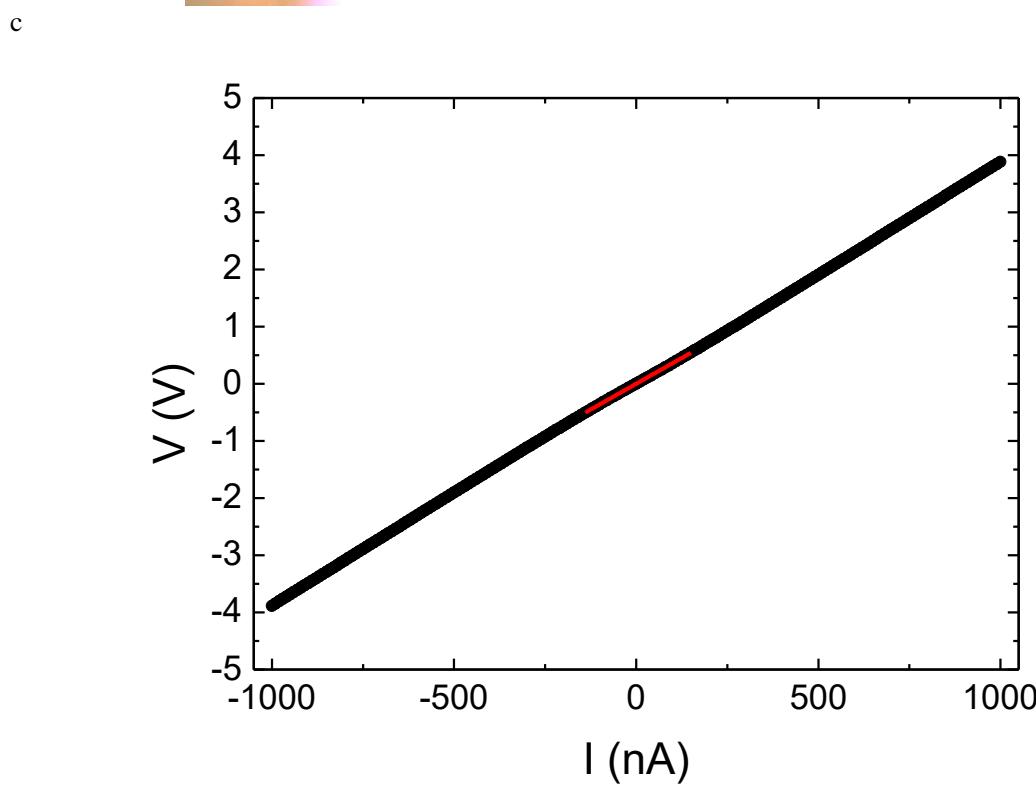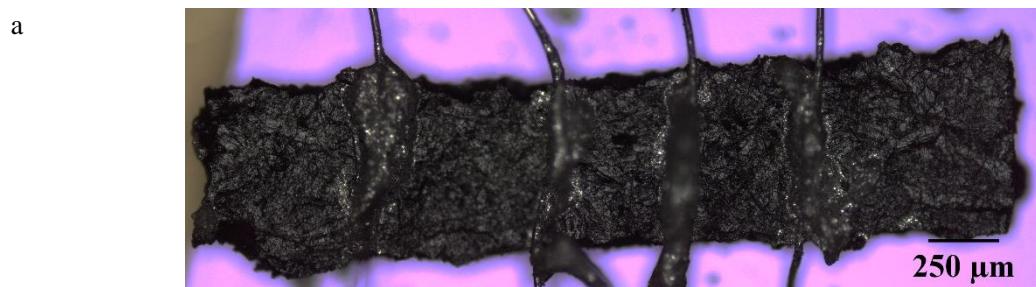


**Figure S24**. Device and electrical response of **MUV-5a(Ho)**#1. a) Top view. b) Lateral view. c) I-V curve at 300 K with the corresponding linear fit (red) of the ohmic regime. The fit gives as a result a slope of $(3.604 \pm 0.005) \cdot 10^6$ $\Omega$ and a y-intercept value of $(-0.0004 \pm 0.0004)$ V, with $R^2 = 0.99995$.
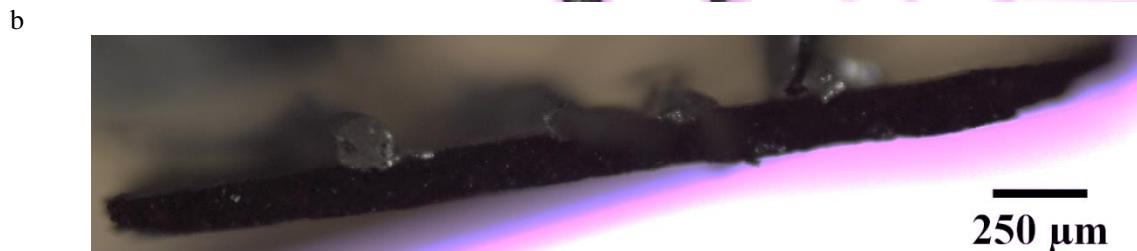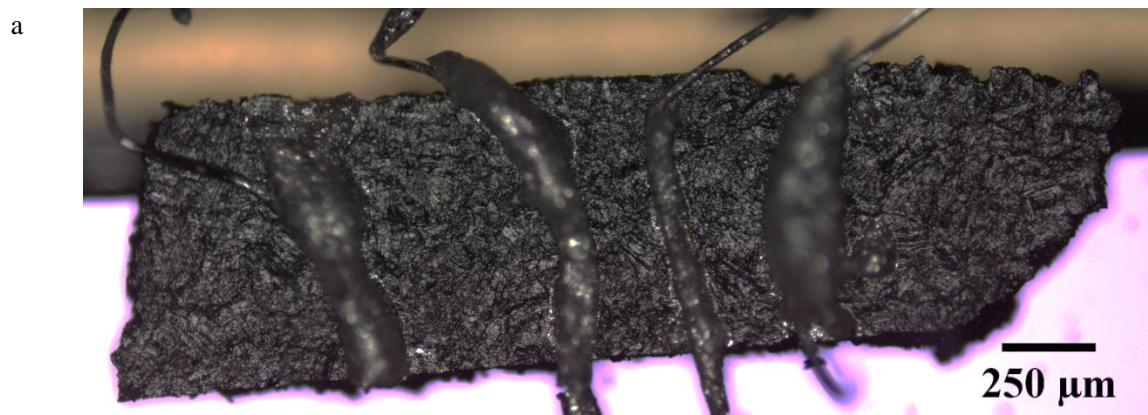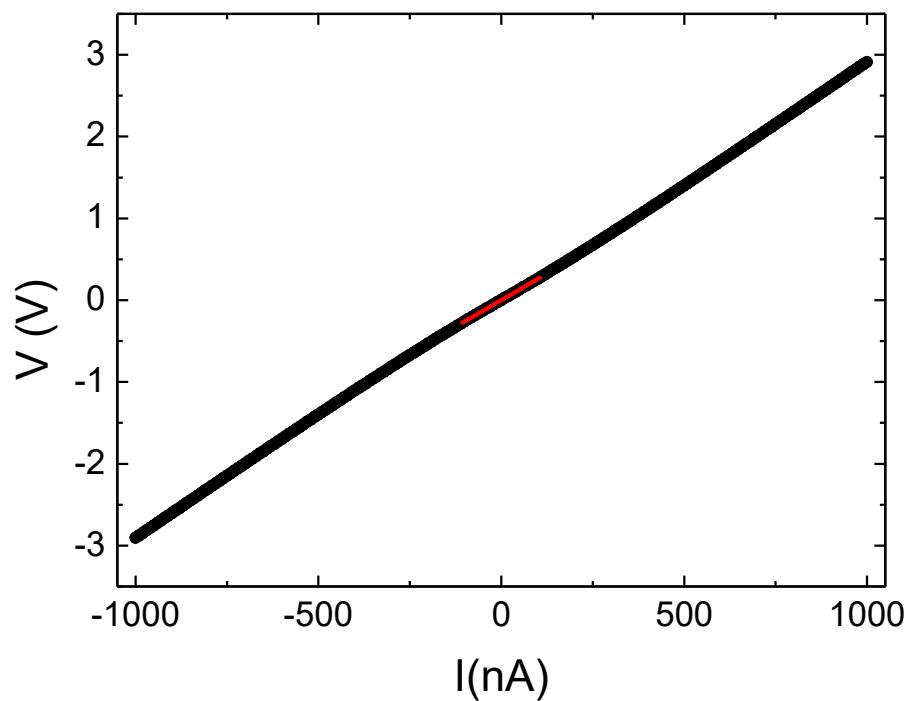
**Figure S25**. Device and electrical response of **MUV-5a(Ho)**#2. a) Top view. b) Lateral view. c) I-V curve at 300 K with the corresponding linear fit (red) of the ohmic regime. The fit gives as a result a slope of $(2.602 \pm 0.002) \cdot 10^6$ $\Omega$ and a y-intercept value of $(0.0051 \pm 0.0015)$ V, with $R^2 = 0.99998$.
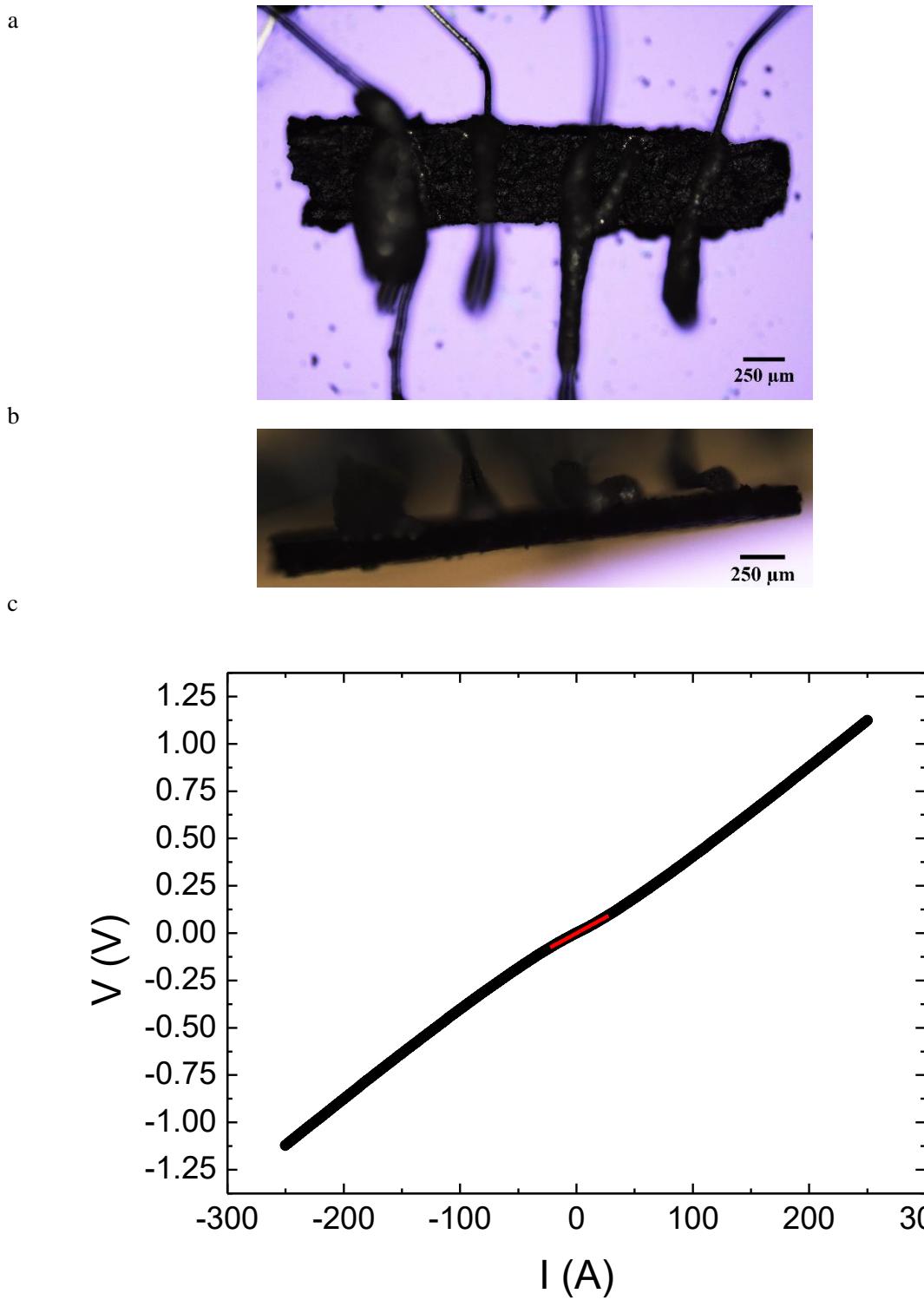
**Figure S26**. Device and electrical response of **MUV-5a(Er)**#1. a) Top view. b) Lateral view. c) I-V curve at 300 K with the corresponding linear fit (red) of the ohmic regime. The fit gives as a result a slope of $(3.347 \pm 0.016) \cdot 10^6$ $\Omega$ and a y-intercept value of $(-0.0003 \pm 0.0002)$ V, with $R^2 = 0.9996$.
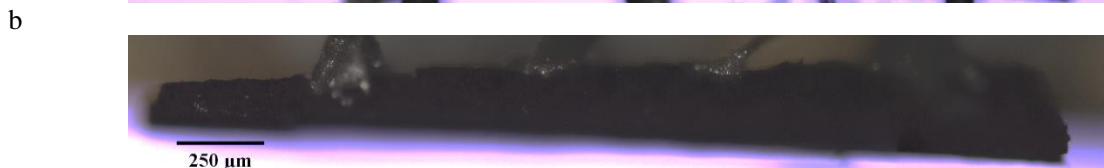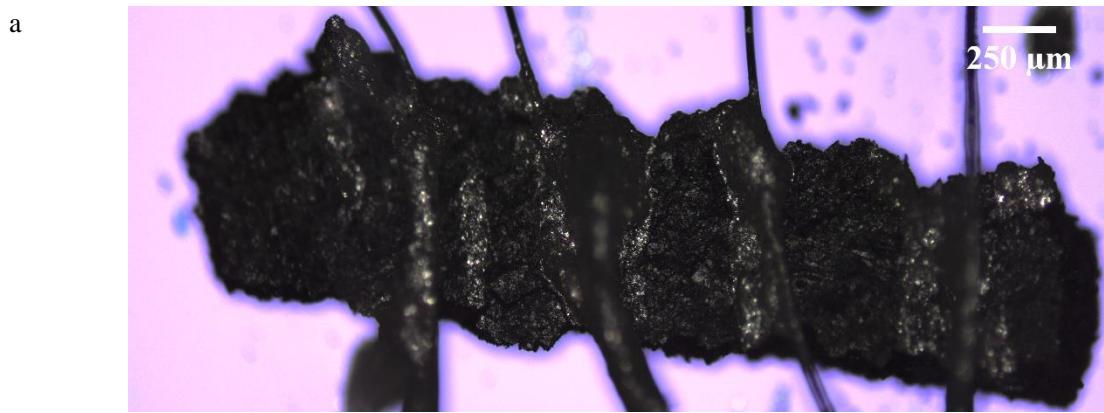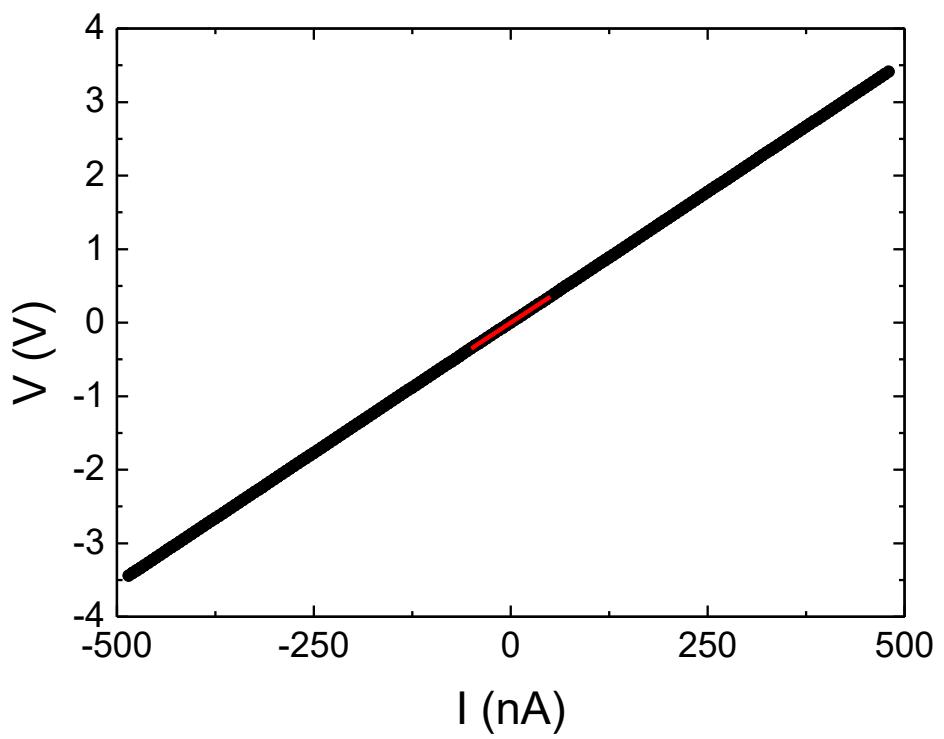
**Figure S27**. Device and electrical response of **MUV-5a(Er)**#2. a) Top view. b) Lateral view. c) I-V curve at 300 K with the corresponding linear fit (red) of the ohmic regime. The fit gives as a result a slope of (7.0164 ± 0.0008)·$10^6$ Ω and a y-intercept value of (-0.0017 ± 0.0008) V, with $R^2$ = 0.99999.
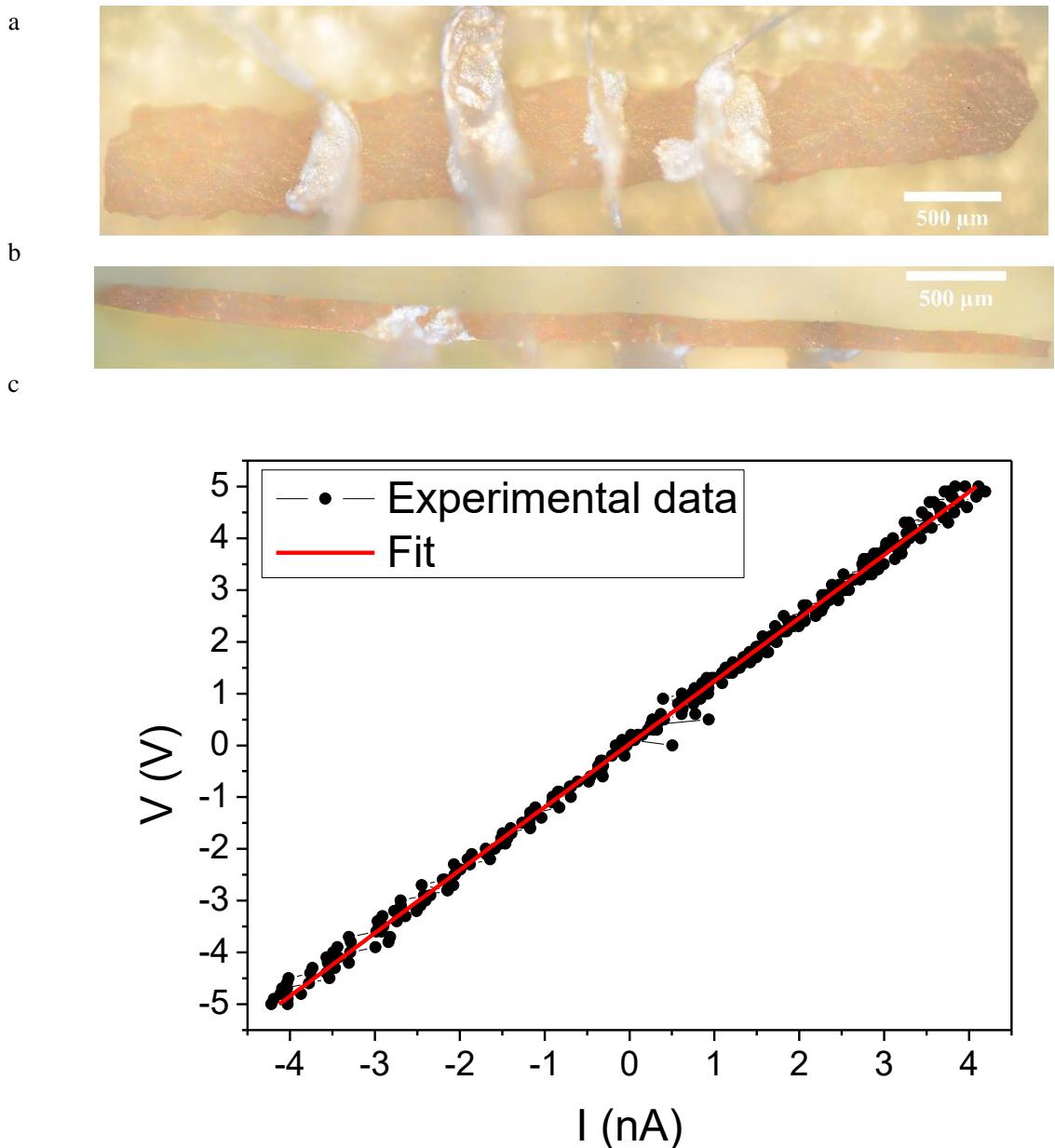
**Figure S28**. Device and electrical response of **MUV-5b(Dy)**#1. a) Top view. b) Lateral view. c) I-V curve at 300 K with the corresponding linear fit (red) of the ohmic regime. The fit gives as a result a slope of $(1.214 \pm 0.004) \cdot 10^9$ $\Omega$ and a y-intercept value of $(0.026 \pm 0.010)$ V, with $R^2 = 0.99688$.

a



b
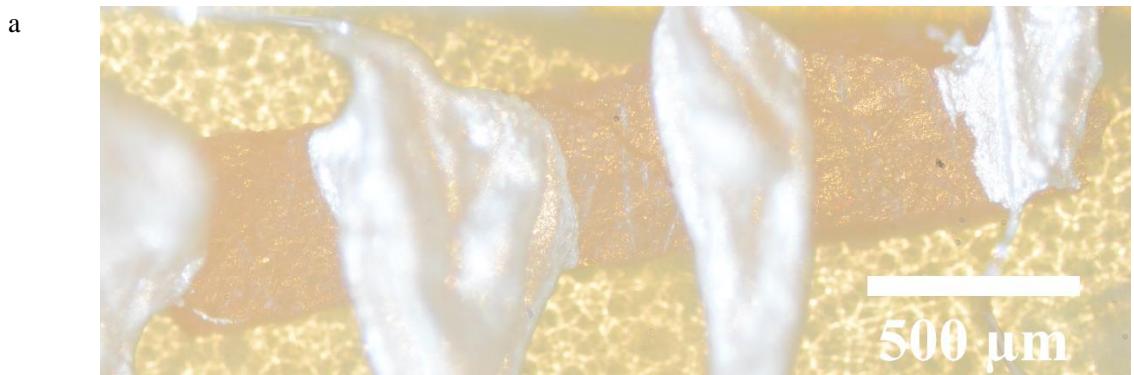


c
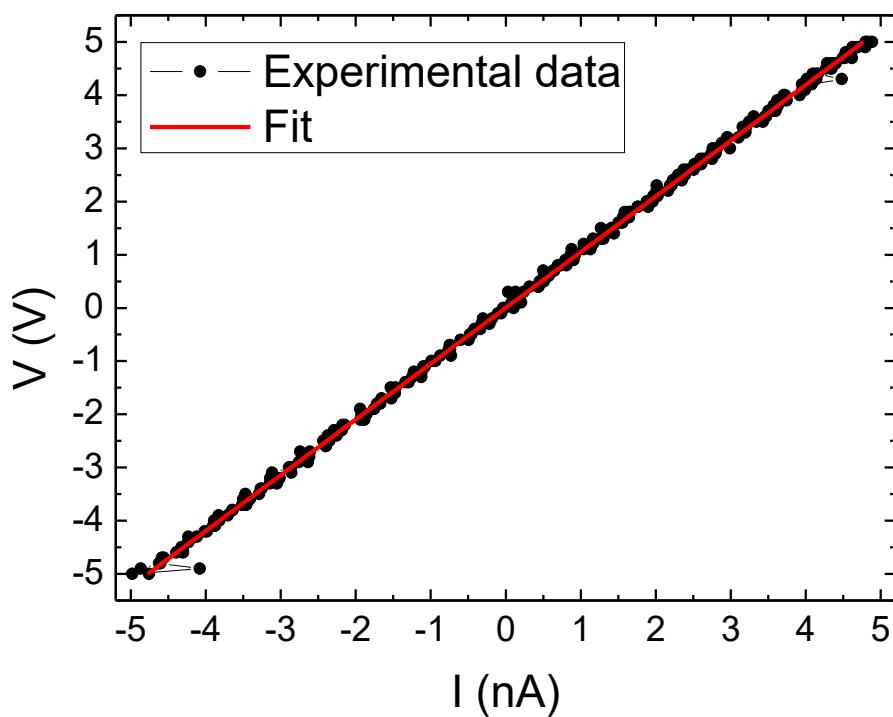


**Figure S29**. Device and electrical response of **MUV-5b(Dy)**#2. a) Top view. b) Lateral view. c) I-V curve at 300 K with the corresponding linear fit (red) of the ohmic regime. The fit gives as a result a slope of $(1.0466 \pm 0.0019) \cdot 10^9$ $\Omega$ and a y-intercept value of $(0.009 \pm 0.005)$ V, with $R^2 = 0.99911$.

**Table S5**. Charge of each moiety of TTF was estimated by using the equation r = 0.762 + 0.049q, where r is the ratio between bond lengths and q is the charge of TTF moieties.[5]

| Compound | Central C=C (Å) | Average C-S (Å) | Ratio, r = L(C=C)/L(C-S) | Charge, q |
|---|---|---|---|---|
| **MUV-5a(Gd)** | 1.388 | 1.737 | 0.799 | 0.755 (± 0.001) |
| **MUV-5a(Tb)** | 1.342 | 1.749 | 0.767 | 0.108 (± 0.001) |
| **MUV-5a(Dy)** | 1.344 | 1.753 | 0.766 | 0.082 (± 0.001) |
| **MUV-5a(Ho)** | 1.353 | 1.749 | 0.773 | 0.224 (± 0.001) |
| **MUV-5a(Er)** | 1.341 | 1.753 | 0.765 | 0.003 (± 0.001) |
| **MUV-5b(Dy)** | 1.320 | 1.760 | 0.750 | N.A. |

The electrochemical experiments were performed using an Autolab electrochemical workstation (Autolab-128N potentiostat/galvanostat) connected to a personal computer that uses Nova 2.1 electrochemical software. The powdered materials (2 mg) were mixed in 2 ml of $CH_3CN$ and deposited on a 3 mm diameter glassy carbon disc working electrode (which was polished sequentially with 0.3, 0.1 and 0.05 ☉m alumina powders and washed with deionised water before each experiment). A typical three-electrode experimental cell equipped with a platinum wire as the counter electrode, and a silver wire as the pseudoreference electrode was used for the electrochemical characterization of the working electrodes. Measurements were carried out with magnetic agitation and nitrogen bubbling. The electrochemical properties were studied measuring the CV at different scan rates in 0.1 M $LiClO_4/CH_3CN$ solution. Ferrocene was added as an internal standard upon completion of the experiment. All potentials are reported in V versus $Fc/Fc^+$.
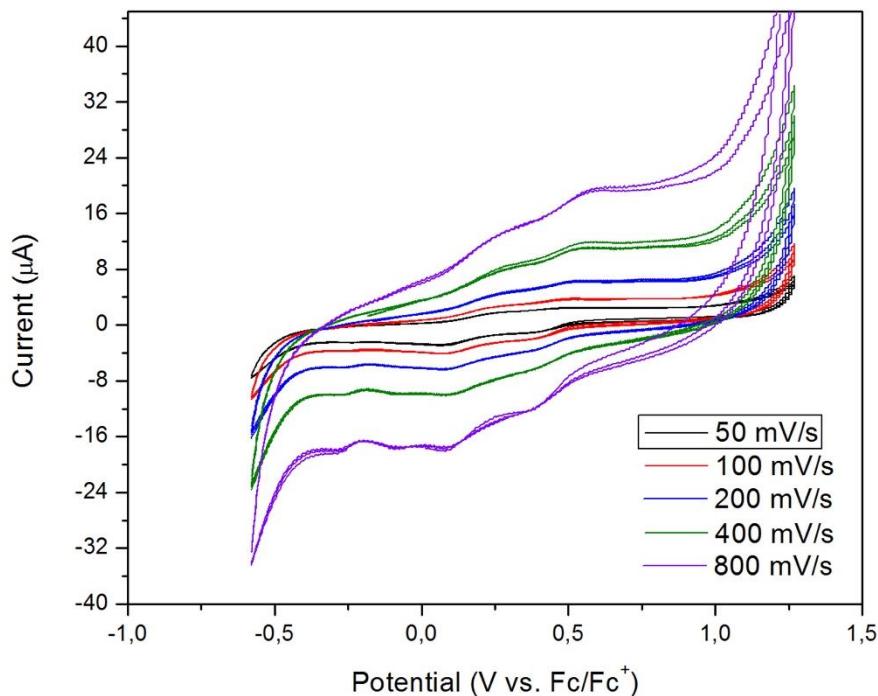


**Figure S30**. Solid-state cyclic voltammetry (CV) of **MUV-5a(Dy)** over three consecutive cycles at different scan rates (50, 100, 200, 400 and 800 mV/s). The experiments were performed at room temperature using Ag as reference electrode, Fc as internal reference and 0.1 M LiClO4 in $CH_3CN$ as electrolyte

## S6. Transfer Integral Calculations
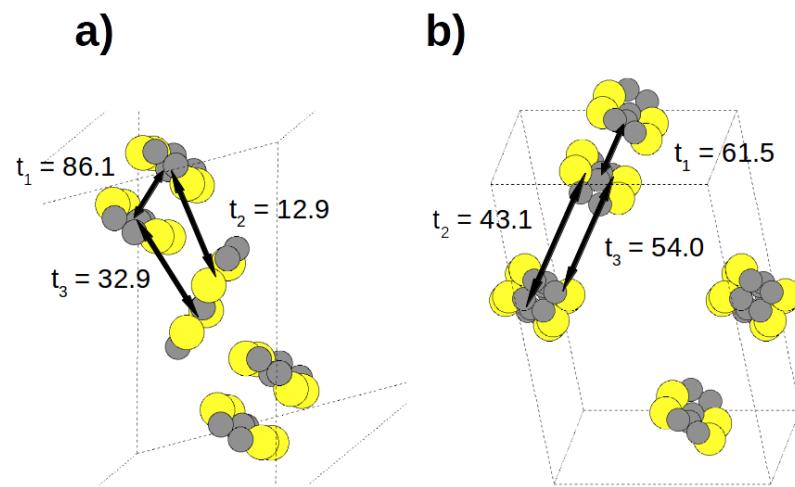


**Figure S31.** Schematic representation of TTF arrangements in the crystal structures of a) ref. [6] and b) ref. [7] indicating the transfer integrals.

**Table S6**. Calculated transfer integrals using B3LYP and PBE0 hybrid functionals

|  | Transfer integrals (meV) | |
|---|---|---|
| **Structure** | **B3LYP** | **PBE0** |
| **MUV-5a** | 16.5 | 15.5 |
|  | 90.6 | 93.3 |
| **MUV-5b** | 8.4 | 9 |
|  | 60.5 | 57.8 |
| **Ref. [6]** | 86.1 | 85.4 |
|  | 32.9 | 27.1 |
|  | 12.9 | 10.2 |
| **Ref. [7]** | 61.5 | 85.2 |
|  | 54 | 40 |
|  | 43.1 | 29.1 |

## S7. Photoluminescence

### Synthesis and characterisation of MUV-5a(Yb$_{0.76}$Er$_{0.24}$)

Synthesis of **MUV-5a(Yb$_{0.76}$Er$_{0.24}$)**: 12 µmol of Yb(CH$_3$COO)$_3$ (4.6 mg), 4 µmol Er(CH$_3$COO)$_3$ (1.4 mg) and 12.5 µmol of H$_4$TTFTB were suspended in a mixture of 1.3 mL of H$_2$O and 0.7 mL of acetic acid (AcOH) in a 4 mL glass vial. The vial was sealed and sonicated for a few minutes to get a homogeneous suspension. The dark suspension was subsequently heated in an oven at 170 ℃ for 12 hours (↑ +2.0 ℃ min$^{-1}$, ↓ -0.4 ℃ min$^{-1}$). After cooling down to room temperature, the dark red crystals were recovered by centrifugation and rinsed with fresh DMF, water and MeOH several times. The solids were then allowed to dry in air at room temperature. The solids were further heated at 150 ℃ for at least 2 hours.
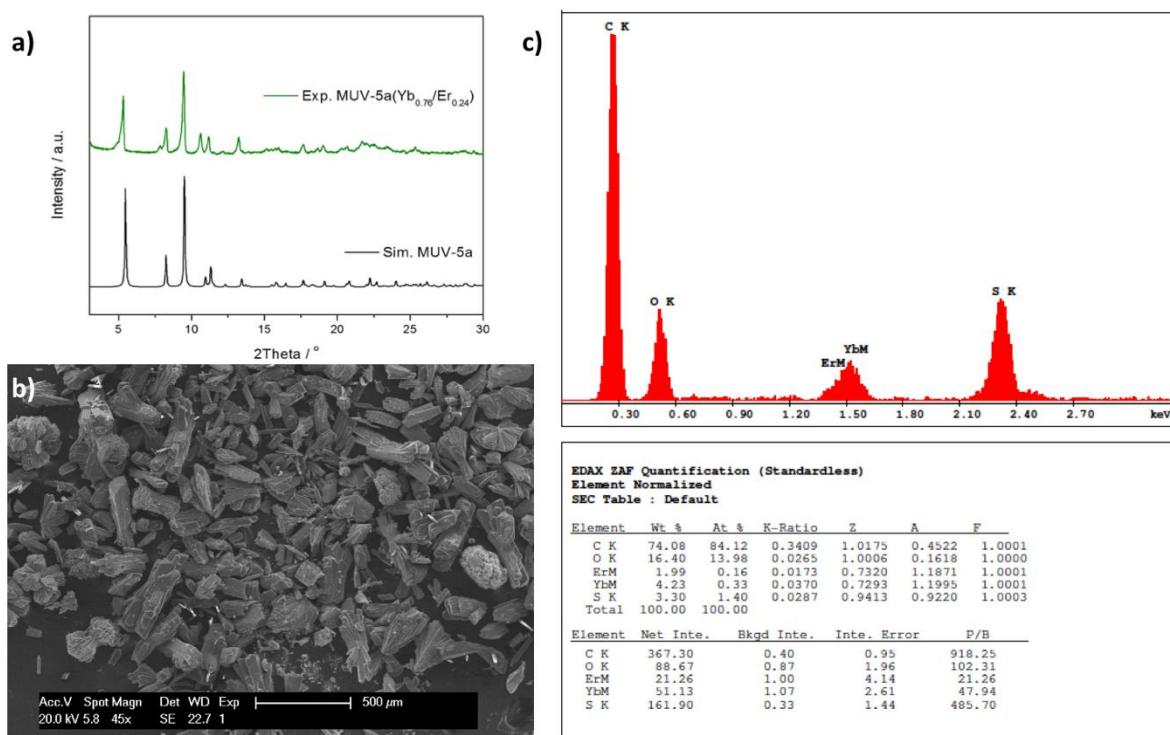


**Figure S32**. a) PXRD of experimental **MUV-5a(Yb$_{0.76}$Er$_{0.24}$)**; b) SEM image of **MUV-5a(Yb$_{0.76}$Er$_{0.24}$)** crystals; and c) EDS analysis of **MUV-5a(Yb$_{0.76}$Er$_{0.24}$)**.

**Table S7**. Determination of Yb/Er ratio in **MUV-5a(Yb/Er)** by ICP-MS (Agilent 7900). The molecular formula was calculated to be **MUV-5a(Yb$_{0.76}$Er$_{0.24}$)**.

| Description | MUV-5(Yb/Er) |
|---|---|
| Er (mg/g) | 42.7 ± 0.8 |
| Yb (mg/g) | 140 ± 2 |

Emission and excitation spectra were recorded on a modular double grating excitation spectrofluorimeter with a TRIAX 320 emission monochromator (Fluorolog-3, Horiba Scientific) coupled to a near infrared H9170 Hamamatsu photomultipliers, using the front face acquisition mode. The excitation source was a 450 W Xe arc lamp. The excitation spectra were corrected for the spectral distribution of the lamp intensity using a photodiode reference detector. Time-resolved measurements were carried out with pulsed Xe-Hg lamp excitation, in front face acquisition mode. The low temperature measurements (12 K) were performed using a helium-closed cycle cryostat with vacuum system measuring ca. $5 \times 10^{-6}$ mbar and a Lakeshore 330 auto-tuning temperature controller with a resistance heater.
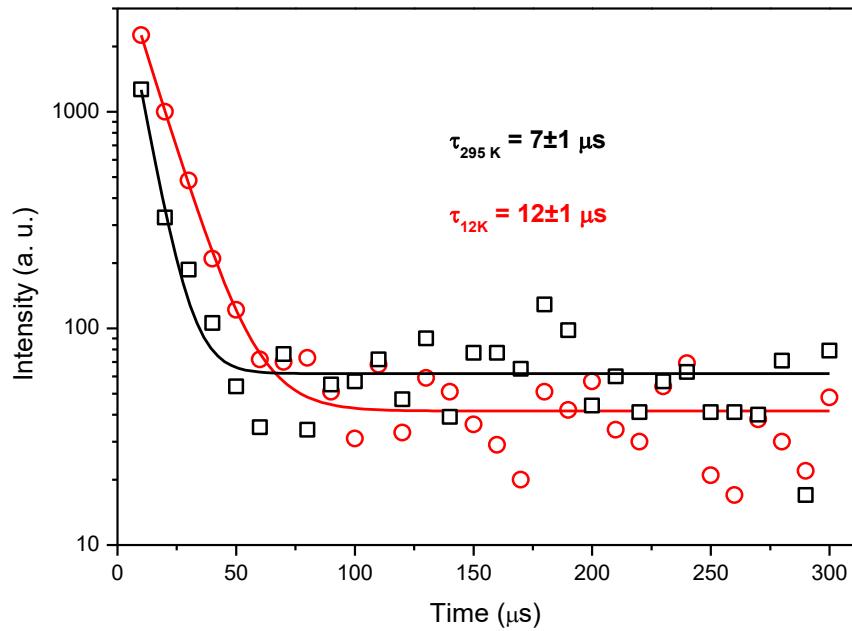


**Figure S33.** $^2F_{7/2}$ decay curve of **MUV-5a(Yb$_{0.76}$Er$_{0.24}$)** acquired at 295 K (black) and at 12 K (red) monitoring the Yb$^{3+}$ emission at 980 nm with the excitation fixed at 560 nm. The solid lines are the best fit using a single exponential decay function ($r^2 > 0.98$ and 0.99 for 295 K and 12 K, respectively). Note that the minimum time discrimination of the phosphorimeter used is 10 µs.

## S8. Magnetic Measurements

Magnetic measurements were performed with a Quantum Design Physical Property Measurement System (PPMS). Variable-temperature (2 – 300 K) direct current (dc) magnetic susceptibility measurements were carried out in an applied field of 1.0 kOe and variable field magnetization measurements up to 5 T at 2.0 K. Variable-temperature (2 – 15 K) alternating current (ac) magnetic susceptibility measurements in a ±4.0 G oscillating field at frequencies in the range of 1– 997 Hz were carried out in a zero dc field and in a dc field of 1.0 kOe.

**AC Measurements**
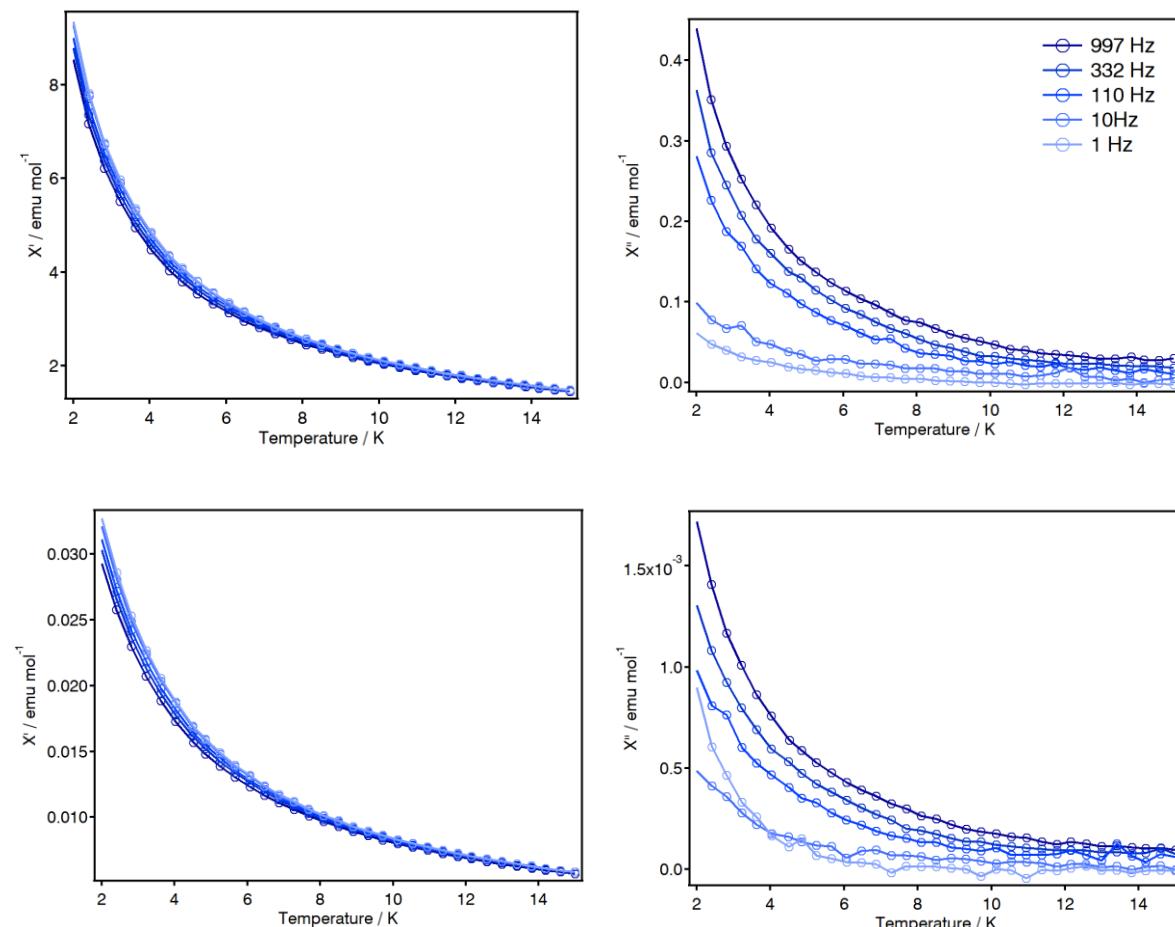


**Figure S34**. In-phase (left) and out-of-phase (right) dynamic magnetic susceptibility of **MUV-5a(Dy)** under an external magnetic field of 0 G (top) and 1000 G (bottom).
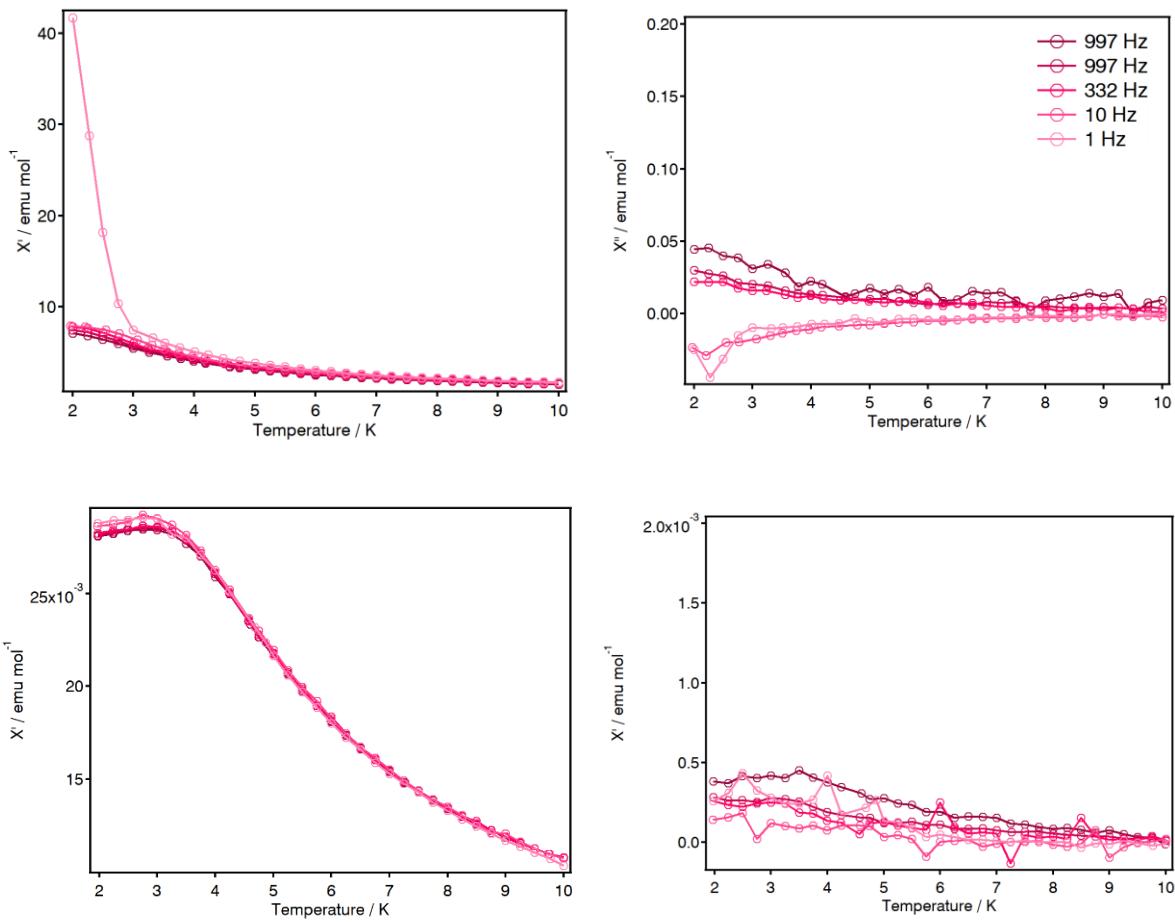
**Figure S35**. In-phase (left) and out-of-phase (right) dynamic magnetic susceptibility of **MUV-5a(Er)** under an external magnetic field of 0 G (top) and 1000 G (bottom).

## Computational Modelling

*Radial Effective Charge (REC) model*: The model is an electrostatic *semi-empirical* crystal field approach commonly used in molecular magnetism, which provides an estimation of the crystal field parameters (CFPs) and permits to rationalize the magnetic properties of a particular *f*-block coordination complex.[8] From the computed CFPs, the model estimates the ground-*J* multiplet energy levels and their corresponding wave functions, which are composed by the different $M_J$ microstates. This kind of calculations use the crystallographic atomic coordinates of the first coordination sphere around the magnetic centre as an input. The software code that has this model implemented is the SIMPRE computational package,[9] which parameterizes the electric field effect produced by the surrounding ligands by using the following Crystal Field Hamiltonian expressed in terms of the Extended Stevens Operators (ESOs).[10]

$$\hat{H}_{cf}(J) = \sum_{k=2,4,6} \sum_{q=-k}^{k} B_k^q O_k^q = \sum_{k=2,4,6} \sum_{q=-k}^{k} a_k (1 - s_k) A_k^q \langle r^k \rangle O_k^q \tag{1}$$

where $k$ is the order (also called rank or degree) and $q$ is the operator range, that varies between $k$ and $-k$, of the Stevens operator equivalents $O_k^q$ as defined by Ryabov in terms of the angular momentum operators $J_{\pm}$ and $J_z$,[11] where the components $O_k^q(c)$ and $O_k^q(s)$ correspond to the ESOs with $q \geq 0$ and $q < 0$ respectively.[12] Note that all the Stevens CF parameters $B_k^q$ are real, whereas the matrix elements of $O_k^q$ ($q < O$) are imaginary. $a_k$ are the $\alpha$, $\beta$ and $\gamma$ Stevens coefficients for $k = 2, 4, 6$, respectively, which are tabulated and depend on the number of *f* electrons. $\sigma_k$ are the Sternheimer shielding parameters of the 4*f* electronic shell, and $<r^k>$ are the expectation values of the radius.[13]

In SIMPRE, the $A_k^q$ CF parameters are determined by the following relations:

$$A_k^0 = \frac{4\pi}{2k+1} \sum_{i=1}^{N} \frac{Z_i e^2}{R_i^{k+1}} Z_{k0}(\theta_i, \varphi_i) p_{kq} \tag{2a}$$

$$A_k^q = \frac{4\pi}{2k+1} \sum_{i=1}^{N} \frac{Z_i e^2}{R_i^{k+1}} Z_{kq}^c(\theta_i, \varphi_i) p_{kq} \qquad (q>0) \tag{2b}$$

$$A_k^q = \frac{4\pi}{2k+1} \sum_{i=1}^{N} \frac{Z_i e^2}{R_i^{k+1}} Z_{k|q|}^s(\theta_i, \varphi_i) p_{k|q|} \qquad (q<0) \tag{2c}$$

where $R_i$, $\theta_i$ and $\varphi_i$ are the effective polar coordinates of the point charges, and $Z_i$ is the effective point charge, associated to the *i*-th donor atom with the lanthanoid at the origin, $N$ is the number of ligands; $e$ is the electron charge, $p_{kq}$ are the prefactors of the spherical harmonics and $Z_{kq}$ are the tesseral harmonics expressed in terms of the polar coordinates for the i-th donor atom.

In the model, the effect of the ligand is reproduced through an effective point charge situated between the lanthanoid and the coordinated atom at a distance $R_i$ from the magnetic centre, which is smaller than the real metal-ligand distance ($r_i$). To account for the effect of covalent electron sharing, a radial displacement vector ($D_r$) is defined, in which the polar coordinate $r$ of each coordinated atom is collectively varied, $R_i = r_i - D_r$, whereas $\theta_i$ and $\varphi_i$ remain constant. In the case of MUV-5a, we have taken advantage of the REC parameters recently obtained for the coordinated O atoms of the carboxylate ligands in MUV-4b ($D_r = 0.885$ Å, $Z_i = 0.1024$),[14] which have allowed a satisfactory reproduction of the magnetic properties of the series by considering the different crystallographic centres. The relative error $E$ is defined as:

$$E = \frac{1}{n} \sum_{i=1}^{n} \frac{\left[ \chi_{theo,i} - \chi_{\exp,i} \right]^2}{\left[ \chi_{\exp,i} \right]^2} \tag{3}$$

where $\chi_{exp}$ and $\chi_{theo}$ are experimental and theoretical magnetic susceptibility, respectively, and $n$ is the number of points.

**Table S8**. Crystal-field parameters ($A_k^q \langle r^k \rangle$; Stevens notation) in cm$^{-1}$ obtained for the two crystallographically independent magnetic centers of **MUV-5a(Ln)**, Ln = Tb, Dy, Ho and Er.

| $k$ | $q$ | Tb1 | Tb2 | Dy1 | Dy2 | Ho1 | Ho2 | Er1 | Er2 |
|---|---|---|---|---|---|---|---|---|---|
| 2 | 0 | -123.38 | -110.40 | -97.52 | 58.41 | 78.89 | 22.71 | -99.46 | -74.71 |
| 2 | 1 | 85.44 | 128.36 | 40.72 | -149.32 | -4.62 | -237.28 | -10.25 | -159.29 |
| 2 | -1 | -93.15 | -42.03 | -162.48 | -314.11 | 6.81 | -272.58 | 110.45 | 152.46 |
| 2 | 2 | 1.57 | -111.35 | 23.29 | -0.41 | 111.82 | 41.45 | 47.09 | -69.12 |
| 2 | -2 | 17.88 | -15.68 | 12.41 | -130.83 | 94.85 | -59.23 | 8.96 | 26.57 |
| 4 | 0 | -16.09 | -69.61 | 94.78 | 56.87 | 37.09 | 59.29 | 69.63 | -55.83 |
| 4 | 1 | -28.26 | -166.73 | 19.64 | 28.23 | -0.90 | 44.39 | -26.79 | 76.40 |
| 4 | -1 | 30.80 | 56.15 | -75.69 | 140.78 | 14.71 | -45.70 | 277.66 | 139.40 |
| 4 | 2 | -45.03 | 88.69 | 40.51 | 47.03 | 278.15 | -23.39 | -77.04 | 258.56 |
| 4 | -2 | -509.52 | -197.16 | 22.01 | 8.21 | 124.62 | -70.58 | -14.70 | 240.92 |
| 4 | 3 | 414.81 | 1323.63 | 814.65 | -97.90 | -57.76 | 27.05 | -282.42 | -484.32 |
| 4 | -3 | 317.20 | 541.15 | -891.09 | -45.55 | -14.75 | 426.03 | 972.37 | 395.01 |
| 4 | 4 | 178.80 | -55.24 | 40.28 | 429.56 | -466.75 | -367.98 | -9.16 | -73.04 |
| 4 | -4 | -31.79 | -26.588 | 60.79 | -405.88 | -49.62 | 442.27 | -3.85 | 154.45 |
| 6 | 0 | -23.97 | 8.73 | 16.60 | -13.01 | 0.77 | -15.48 | 9.93 | 1.51 |
| 6 | 1 | 5.76 | 11.42 | -1.84 | -56.44 | 6.86 | 23.26 | -7.22 | 15.11 |
| 6 | -1 | -6.26 | -80.98 | 8.31 | -40.24 | -0.42 | 1.24 | 75.30 | -29.21 |
| 6 | 2 | 4.11 | -101.86 | -14.46 | -22.06 | 106.23 | 2.91 | 37.25 | -20.13 |
| 6 | -2 | 46.61 | 70.67 | -7.95 | 5.37 | -55.50 | 34.36 | 6.91 | -8.69 |
| 6 | 3 | 39.97 | 185.76 | -230.00 | -51.07 | 2.36 | -45.69 | 79.18 | -262.90 |
| 6 | -3 | 30.53 | 34.23 | 251.74 | -24.97 | 15.18 | -8.13 | -272.90 | 146.59 |
| 6 | 4 | -104.64 | -39.59 | -51.94 | -71.74 | 146.22 | 63.97 | -29.09 | -24.07 |
| 6 | -4 | 18.61 | 101.89 | -78.39 | 40.71 | 32.42 | -103.90 | -11.36 | 52.53 |
| 6 | 5 | 204.14 | 161.93 | 185.29 | -633.87 | -15.54 | 474.37 | -47.93 | -189.91 |
| 6 | -5 | -321.95 | 60.38 | -65.27 | -102.96 | 9.14 | 82.19 | 94.30 | 56.23 |
| 6 | 6 | 24.58 | 12.55 | -3.56 | -36.04 | 111.95 | 0.56 | -7.36 | -12.66 |
| 6 | -6 | 90.91 | -27.40 | -39.95 | -25.03 | 6.41 | -29.54 | -4.66 | 51.30 |

**Table S9**. Ground multiplet energy level scheme (in cm$^{-1}$) and main |M$_J$> contributions (> 10%) to the wave function calculated for **MUV-5a(Tb1)** and **MUV-5a(Tb2)**.

| | MUV-5a(Tb1) | | MUV-5a(Tb2) |
|---|---|---|---|
| **0** | 59.3% |0> + 19.0% |+2> + 19.0% |-2> | **0.0** | 66.9% |0> |
| **0.3** | 46.1% |+1> + 46.1% |-1> | **2.6** | 41.9% |+1> + 41.9% |-1> |
| **60** | 18.5% |+4> + 18.5% |-4> | **48** | 30.5% |+1> + 30.5% |-1> |
| **63** | 21.9% |+2> + 21.9% |-2> + 17.4% |+4> + 17.4% |-4> | **66** | 36.2% |+2> + 36.2% |-2> |
| **69** | 19.6% |+3> + 19.6% |-3> + 14.0% |+5> + 14.0% |-5> | **86** | 26.2% |+2> + 26.2% |-2> |
| **72** | 29.7% |+3> + 29.7% |-3> + 16.3% |+5> + 16.3% |-5> | **102** | 20.1% |+3> + 20.1% |-3> + 19.9% |+6> + 19.9% |-6> |
| **113** | 34.4% |+1> + 34.4% |-1> | **113** | 29.5% |+6> + 29.5% |-6> |
| **123** | 26.3% |+2> + 26.3% |-2> + 13.5% |+4> + 13.5% |-4> | **153** | 21.8% |+3> + 21.8% |-3> |
| **134** | 23.9% |0> + 17.3% |+2> + 17.3% |-2> | **164** | 20.5% |+3> + 20.5% |-3> + 16.2% |+6> + 16.2% |-6> + 10.4% |+4> + 10.4% |-4> |

| | | | |
|---|---|---|---|
| **189** | 26.2% \|+5> + 26.2% \|-5> + 13.5% \|+3> + 13.5% \|-3> | **204** | 19.8% \|+4> + 19.8% \|-4> + 12.0% \|+5> + 12.0% \|-5> |
| **191** | 25.0% \|+5> + 25.0% \|-5> + 12.7% \|+3> + 12.7% \|-3> | **208** | 22.6% \|+4> + 22.6% \|-4> + 11.7% \|+5> + 11.7% \|-5> |
| **256** | 26.0% \|+6> + 26.0% \|-6> + 13.8% \|+4> + 13.8% \|-4> | **253** | 24.8% \|+5> + 24.8% \|-5> + 11.2% \|+4> + 11.2% \|-4> |
| **257** | 26.0% \|+6> + 26.0% \|-6> + 14.3% \|+4> + 14.3% \|-4> | **253** | 24.7% \|+5> + 24.7% \|-5> + 11.5% \|+4> + 11.5% \|-4> |

**Table S10**. Ground multiplet energy level scheme (Kramers doublets in cm$^{-1}$) and main \|M$_J$> contributions (> 10%) to the wave function calculated for **MUV-5a(Dy1)** and **MUV-5a(Dy2)**.

| MUV-5a(Dy1) | | MUV-5a(Dy2) | |
|---|---|---|---|
| **0** | 98.7% \|±1/2> | **0** | 80.0% \|±15/2> |
| **31** | 94.0% \|±3/2> | **29** | 25.6% \|±5/2> + 15.6% \|∓3/2> + 14.2% \|±3/2> |
| **70** | 40.9% \|±15/2> + 28.2% \|±5/2> + 10.9% \|±13/2> + 10.3% \|±9/2> | **42** | 20.6% \|±1/2> + 16.2% \|±7/2> + 13.5% \|±9/2> + 12.7% \|∓1/2> |
| **83** | 55.9% \|±5/2> + 22.2% \|±15/2> | **101** | 28.2% \|±13/2> + 15.1% \|±11/2> + 15.3% \|∓3/2> |
| **102** | 44.1% \|±7/2> + 33.2% \|±13/2> + 14.9% \|±15/2> | **118** | 20.8% \|±9/2> + 19.8% \|±13/2> + 14.5% \|±11/2> + 11.0% \|±7/2> |
| **203** | 36.0% \|±11/2> + 25.4% \|±7/2> + 16.7% \|±9/2> + 15.6% \|±13/2> | **154** | 23.7% \|±13/2> + 14.5% \|±5/2> + 11.2% \|∓1/2> + 10.6% \|∓11/2> |
| **241** | 63.8% \|±9/2> + 17.2% \|±11/2> + 11.6% \|±15/2> | **205** | 19.2% \|±11/2> + 16.1% \|±5/2> + 12.1% \|±9/2> + 10.6% \|±13/2> |
| **247** | 34.9% \|±13/2> + 31.0%\|±11/2> + 19.7% \|±7/2> | **290** | 20.0% \|±9/2> + 18.1% \|±11/2> + 13.0% \|±7/2> + 10.5% \|±3/2> + 10.1% \|±1/2> |

**Table S11**. Ground multiplet energy level scheme (Kramers doublets in cm$^{-1}$) and main \|M$_J$> contributions (> 10%) to the wave function calculated for **MUV-5a(Ho1)** and **MUV-5a(Ho2)**.

| MUV-5a(Ho1) | | MUV-5a(Ho2) | |
|---|---|---|---|
| **0.0** | 29.3% \|+8> + 29.3% \|-8> + 12.4% \|+6> + 12.4% \|-6> | **0.0** | 71.6% \|0> |
| **2.4** | 32.5% \|+8> + 32.5% \|-8> + 13.9% \|+6> + 13.9% \|-6> | **1.2** | 32.4% \|+1> + 32.4% \|-1> |
| **16** | 25.5% \|+3> + 25.5% \|-3> + 19.8% \|+1> + 19.8% \|-1> | **6** | 22.4% \|+1> + 22.4% \|-1> + 10.5% \|+2> + 10.5% \|-2> |
| **19** | 43.9% \|+2> + 43.9% \|-2> | **10** | 24.5% \|+2> + 24.5% \|-2> + 11.4% \|+1> + 11.4% \|-1> |
| **37** | 23.6% \|+1> + 23.6% \|-1> + 14.5% \|+3> + 14.5% \|-3> | **48** | 37.6% \|+7> + 37.6% \|-7> |
| **48** | 54.6% \|0> + 15.1% \|+4> + 15.1% \|-4> | **66** | 23.1% \|+7> + 23.1% \|-7> + 17.1% \|+8> + 17.1% \|-8> |
| **61** | 27.6% \|+7> + 27.6% \|-7> + 18.7% \|+5> + 18.7% \|-5> | **82** | 35.1% \|+8> + 35.1% \|-8> |
| **68** | 31.2% \|+7> + 31.2% \|-7> | **87** | 28.8% \|+8> + 28.8% \|-8> + 13.7% \|+7> + 13.7% \|-7> |
| **128** | 33.3% \|+4> + 33.3% \|-4> | **109** | 26.4% \|+6> + 26.4% \|-6> |
| **136** | 18.1% \|+5> + 18.1% \|-5> + 12.1% \|+1> + 12.1% \|-1> | **123** | 37.1% \|+6> + 37.1% \|-6> |
| **151** | 15.1% \|+6> + 15.1% \|-6> + 12.0% \|+8> + 12.0% \|-8> + 10.2% \|+2> + 10.2% \|-2> | **148** | 19.3% \|+5> + 19.3% \|-5> + 11.2% \|+4> + 11.2% \|-4> |

| 166 | 29.9% \|+6> + 29.9% \|-6> + 10.0% \|+8> + 10.0% \|-8> | 170 | 22.4% \|+5> + 22.4% \|-5> + 15.7% \|+2> + 15.7% \|-2> |
|---|---|---|---|
| 173 | 24.9% \|+5> + 24.9% \|-5> + 15.4% \|+7> + 15.4% \|-7> | 175 | 29.5% \|+4> + 29.5% \|-4> |
| 180 | 19.2% \|+3> + 19.2% \|-3> + 12.9% \|+1> + 12.9% \|-1> | 178 | 21.6% \|+3> + 21.6% \|-3> |
| 182 | 17.5% \|+6> + 17.5% \|-6> + 17.3% \|+2> + 17.3% \|-2> | 181 | 19.7% \|+5> + 19.7% \|-5> + 10.6% \|+3> + 10.6% \|-3> |
| 195 | 21.3% \|0> + 16.8% \|+2> + 16.8% \|-2> + 18.9% \|+4> + 18.9% \|-4> | 206 | 22.0% \|+3> + 22.0% \|-3> + 14.0% \|+5> + 14.0% \|-5> |
| 195 | 15.8% \|+1> + 15.8% \|-1> | 210 | 35.0% \|+4> + 35.0% \|-4> + 12.6% \|0> |

**Table S12**. Ground multiplet energy level scheme (Kramers doublets in $cm^{-1}$) and main $|M_J>$ contributions (> 10%) to the wave function calculated for **MUV-5a(Er1)** and **MUV-5a(Er2)**.

| | MUV-5a(Er1) | | MUV-5a(Er2) |
|---|---|---|---|
| **0** | 80.1% \|±13/2> + 11.7% \|±15/2> | **0** | 66.6% \|±15/2> + 19.0% \|±9/2> |
| **11** | 55.7% \|±11/2> + 20.4% \|±9/2> | **25** | 26.2% \|±1/2> + 14.9% \|±3/2> + 11.3% \|±7/2> |
| **27** | 38.9% \|±9/2> + 14.8% \|±7/2> + 12.5% \|±11/2> + 10.3% \|±3/2> | **38** | 41.9% \|±13/2> + 13.3% \|±7/2> |
| **50** | 29.1% \|±1/2> + 21.8% \|±7/2> + 11.1% \|±11/2> | **81** | 29.1% \|±11/2> + 15.7% \|∓3/2> + 11.9% \|±13/2> + 10.3% \|±7/2> |
| **120** | 38.7% \|±5/2> + 22.3% \|∓7/2> + 11.9% \|±3/2> | **116** | 25.7% \|±5/2> + 25.2% \|±3/2> + 14.5% \|±9/2> + 13.2% \|±11/2> |
| **139** | 37.1% \|±15/2> + 33.1% \|±3/2> | **142** | 33.6% \|±1/2> + 22.1% \|±5/2> + 12.1% \|∓3/2> |
| **171** | 42.1% \|±15/2> + 19.6% \|±9/2> + 10.9% \|±3/2> + 10.5% \|±5/2> | **192** | 32.5% \|±7/2> + 29.1% \|±11/2> |
| **187** | 29.8% \|±1/2> + 14.6% \|∓1/2> + 13.0% \|±7/2> + 10.7% \|∓3/2> | **199** | 42.7% \|±9/2> + 22.0% \|±13/2> + 10.6% \|±7/2> |

## S9. References

[1] Nowell H, Barnett SA, Christensen KE, Teat SJ, Allan DR. *J Synchrotron Radiat.*, **2012**, *19,* 435-441.

[2] (a) G. M. Sheldrick, SADABS, empirical absorption correction program based upon the method of Blessing. (b) L. Krause, R. Herbst-Irmer, G. M. Sheldrick, D. Stalke, An empirical correction for absorption anisotropy *J. Appl. Cryst.* **2015**, *48*. (c) R. H. Blessing, An empirical correction for absorption anisotropy, *Acta Crystallogr.* **1995**, *A51*, 33-38.

[3] a) Sheldrick. G. M. Crystal structure refinement with SHELXL, *Acta Crystallogr.*, **2015**, *C71*, 3-8;

[4] O. V. Dolomanov, L. J. Bourhis, R. J. Gildea, J. A. K. Howard, H. Puschmann, OLEX2: a complete structure solution, refinement and analysis program. *J. Appl. Cryst.*, **2009**, *42*, 339–341.

[5] T. C. Umland, S. Allie, T. Kuhlmann, P. Coppens, *J. Phys. Chem.* **1988**, *92*, 6456–6460.

[6] L. S. Xie, M. Dinca, *Isr. J. Chem.* **2018**, *2139*, 1119–1122.

[7] J. Su, T. Hu, R. Murase, H. Wang, D. M. D. Alessandro, M. Kurmoo, J. Zuo, *Inorg. Chem.* **2019**, *58*, 3698–3706.

[8] J.J. Baldoví, J.J. Borrás-Almenar, J.M. Clemente-Juan, E. Coronado, A. Gaita-Ariño, *Dalton Trans.* **2012**, *41*, 13705.

[9] J.J. Baldoví, S. Cardona-Serra, J.M. Clemente-Juan, E. Coronado, A. Gaita-Ariño, A. Palii, *J. Comput. Chem.,* **2013**, *34*, 1961.

[10] (a) C. Rudowicz, C.Y. Chung, *J. Phys. Condens. Matter*, **2004**, *16*, 5825; (b) C. Rudowicz, *J. Phys. C: Solid State Phys.*, **1985**, *18*, 1415; (c) C. Rudowicz, *J. Phys. C: Solid State Phys.*, **1985**, *18*, 3837 (erratum).

[11] I.D. Ryabov, *Journal of Magnetic Resonance*, **1999**, *140*, 141.

[12] K. W. H. Stevens, *Proc.Phys. Soc.* **1952**, *65*, 209.

[13] S. Edvardsson, M. Klinterberg, *Journal of Alloys and Compounds,* **1998**, *275*, 233.

[14] J. Castells-Gil, J. J. Baldoví, Carlos Martí-Gastaldo, G. Mínguez Espallargas, *Dalt. Trans.* **2018**, *47*, 14734–14740.